CHALMERS
UNIVERSITY OF TECHNOLOGY

Experimental investigation of the flowability of oxygen carriers for Chemical-Looping Combustion

Master's thesis in Energy Science and Engineering

Tobias Herrmann

Department of Energy and Environment
Division of Energy Technology
CHALMERS UNIVERSITY OF TECHNOLOGY
Gothenburg, Sweden 2015

Master's thesis 2015

Experimental investigation of the flowability of oxygen carriers for Chemical-Looping Combustion

Tobias Herrmann

CHALMERS
UNIVERSITY OF TECHNOLOGY

Department of Energy and Environment
Division of Energy Technology
Chemical-Looping Combustion
Chalmers University of Technology
Gothenburg, Sweden 2015

Experimental investigation of the flowability of different oxygen carriers for Chemical-Looping Combustion
Tobias Herrmann

Supervisor: Carl Johan Linderholm, Department of Energy and Environment
Examiner: Magnus Ryden, Department of Energy and Environment

Master's Thesis 2015
Department of Energy and Environment
Division of Energy Technology
Chemical Looping Combustion
Chalmers University of Technology
SE-412 96 Gothenburg
Telephone +46 31 772 1000

Typeset in LaTeX
Printed by Chalmers Reproservice
Gothenburg, Sweden 2015

Experimental investigation of the flowability of oxygen carriers for Chemical-Looping Combustion

Tobias Herrmann
Department of Energy and Environment
Division of Energy Technology
Chalmers University of Technology

Abstract

Chemical-Looping Combustion is a technology which addresses carbon dioxide sequestration in an innovative way. Air and fuel are separately handled in two fluidized bed reactors. Interconnection and reaction are achieved by circulating an oxygen carrier between both reactors. The oxygen carrier is a crucial component, as it is responsible for the performance of the overall process. As the carrier is consistently oxidized in the air reactor and reduced in the fuel rector, a high reaction rate and a high oxygen ratio are required. Furthermore the melting point has to be sufficiently high and solid carbon formation should not be catalysed. Besides these chemical properties, the mechanical nature of the material must be taken into account. Attrition is the process when the material undergoes fragmentation in smaller particles and is consequently elutriated from the system. This has to be avoided since it can decrease the lifetime of the carrier significantly. Another important aspect is the flowability of the carrier which is investigated in this work. The bulk of oxgen carrier would ideally behave as a fluid, flowing freely through the CLC unit. However, the actual CLC environment is not ideal. The flow behavior is altered by phenomenons like clogging or slugging. Because flowability describes the global behaviour of a granular system, which is influenced by a variety of parameters, material investigations as well as simple experiments were conducted. Investigated material properties are related to size, shape, density and surface characteristics. The experimental part consisted of measurements of a flow through a funnel, the Angle of Repose, the Hausner Ratio and the minimum fluidization velocity.

Keywords: Chemical-Looping Combustion, Flowability, Oxygen carrier, Funnel flow, Angle of Repose, Hausner Ratio, Minimum fluidization velocity.

Acknowledgments

The thesis is part of my master's degree at TU Darmstadt and was conducted in the division of Energy Technology at the Chalmers University.
I would like to express my gratitude to all people who have supported me in realizing the project during the last months. Especially my supervisor Carl and my examiner Magnus from Chalmers have earned greatest tribute for their excellent collaboration and guidance throughout the project. They are with Jochen Ströhle and Prof. Bernd Epple from TU Darmstadt responsible for initiating this work and providing this exciting task. I felt always very appreciated and included in the division and especially in the CLC group. All members had great experience and knowledge, which they were not reluctant to share with me. Being part the team and immersing into the complex CLC research made the time here truly memorable. Furthermore I owe Ulf a great "Donnerwetter" for practical help in the lab and his peculiar German expressions. Last but not least I want to thank my dear colleagues in the office and all the people I met during lunch and fika breaks for inspiring and diverting talks. I particularly appreciated the company of Anna, who stayed next to me in the office, even after she graduated and summer set Sweden into paralysis.

Tobias Herrmann, Gothenburg, September 2015

Contents

List of Figures **xii**

List of Tables **xiii**

Nomenclature **xvi**

1 Introduction **1**
1.1 Carbon dioxide - today's worst enemy? . . . 1
1.2 CCS - a strategy for mitigation . . . 2
1.3 Chemical-Looping Combustion - a game changer? . . . 2
1.4 The oxygen carrier - backbone of CLC . . . 3

2 Understanding Flowability **5**
2.1 Approach . . . 5
2.2 Continuum mechanics . . . 5
2.3 Adhesive forces . . . 6

3 Investigating flowability **11**
3.1 Rationale . . . 11
3.2 Oxygen carrier selection . . . 12
3.3 Experimental work . . . 14
3.3.1 Sieving . . . 14
3.3.1.1 Background . . . 14
3.3.1.2 Setup & Procedure . . . 14
3.3.1.3 Analysis . . . 14
3.3.1.4 Results . . . 18
3.3.2 Microscopy . . . 20
3.3.2.1 Background . . . 20
3.3.2.2 Setup & Procedure . . . 20
3.3.2.3 Analysis . . . 20
3.3.2.4 Results . . . 21
3.3.3 Hausner Ratio . . . 23
3.3.3.1 Background . . . 23
3.3.3.2 Setup & Procedure . . . 23
3.3.3.3 Analysis . . . 24
3.3.3.4 Results . . . 24
3.3.4 Funnel Flow . . . 28

3.3.4.1 Background 28
3.3.4.2 Setup & Procedure 29
3.3.4.3 Analysis 30
3.3.4.4 Results 30
3.3.5 Angle of Repose 33
3.3.5.1 Background 33
3.3.5.2 Setup & Procedure 33
3.3.5.3 Analysis 33
3.3.5.4 Results 35
3.3.6 Minimum Fluidization Velocity 37
3.3.6.1 Background 37
3.3.6.2 Setup & Procedure 38
3.3.6.3 Analysis 39
3.3.6.4 Results 40

4 Overall results **43**

5 Conclusion **49**

References **51**

A Appendix A **I**

B Appendix B **V**

C Appendix C **IX**

List of Figures

1.1 Atmospheric CO_2 concentration from 1960 to 2014 from Mauna Loa Observatory, Hawaii [1] . . . 1
1.2 Principle of Chemical-Looping Combustion . . . 3

2.1 a. Schematic setup of an experimental viscosity measurement b. Stress-strain relationship for Powder and Fluid [12] . . . 6
2.2 Influence of particle size on adhesive forces . . . 7
2.3 Particles covered with flow agent . . . 8
2.4 Influence of the size of the agent on adhesive forces . . . 8

3.1 Mass fraction and frequency curve of C14:F . . . 16
3.2 Cumulative distribution curves of C14:F . . . 16
3.3 Results from sieving analysis . . . 18
3.4 Grain size after the sieving process . . . 19
3.5 Image analysis using JMicroVision . . . 21
3.6 Particle images from light microscopy using DFF . . . 22
3.7 Compactness . . . 22
3.8 Tapped density of fresh and used carriers . . . 25
3.9 Tapped density of remaining carriers . . . 25
3.10 Hausner Ratio of non-sieved material . . . 26
3.11 Hausner Ratio of sieved material . . . 27
3.12 Hausner Ratio of remaining carriers . . . 27
3.13 Hausner Ratio of blends and of used SinFin . . . 28
3.14 Flow pattern during discharge . . . 29
3.15 Funnel arrangement for flow time measurements . . . 29
3.16 Funnel flow pattern . . . 30
3.17 A rathole . . . 31
3.18 Funnel flow time measurements . . . 32
3.19 Flow time measurements of remaining carriers and blends . . . 32
3.20 Setup for the experimental determination of the Angle of Repose . . . 34
3.21 Measuring the Angle of Repose . . . 34
3.22 Results of the AOR measurements (1) . . . 35
3.23 Results of the AOR measurements (2) . . . 36
3.24 Δp-versus-u_o for uniformly sized sharp sand [24] . . . 37
3.25 Geldart classification of particles for air at ambient conditions [24] . . . 38
3.26 Δp-versus-u_o for used Ilmenite . . . 39
3.27 Experimental vs calculated u_{mf} values (1) . . . 41

3.28 Experimental vs calculated u_{mf} values (2) 42

4.1 Flowability score (AOR, Flow, HR) 45
4.2 Flowability score (AOR, Flow, HR) 45
4.3 Correlation analysis 47

C.1 Flowability score (AOR, Flow, HR, u_{mf}) X
C.2 Flowability score (AOR, Flow, HR, u_{mf}) X

List of Tables

3.1 Investigated oxygen carriers 13
3.2 Obtained data from sieving [C14:F] 15
3.3 Obtained data from sieving [C14:F] 17
3.4 u_{mf}: particle properties and results for fresh material 40
3.5 u_{mf}: particle properties and results for used material 41

4.1 Values for derivation of the flowability score 44
4.2 Mean and standard deviation 44
4.3 Scores 44

A.1 PSD Data non-sieved II
A.2 PSD Data sieved III

B.1 Experimental Outcome - non-sieved fresh VI
B.2 Scores - non-sieved fresh VI
B.3 Experimental Outcome - non-sieved used VI
B.4 Scores - non-sieved used VII
B.5 Experimental Outcome - sieved fresh VII
B.6 Scores - sieved fresh VII
B.7 Experimental Outcome - sieved used VIII
B.8 Scores - sieved used VIII

C.1 Values for derivation of the flowability score IX
C.2 Mean and standard deviation IX
C.3 Scores IX

Nomenclature

Acronyms

AOR	angle of repose
CCS	carbon capture and storage
CLC	chemical-looping combustion
HR or H_r	Hausner ratio
ppm	parts per million
PSD	particle size distribution

Symbols

Symbol	Units	Description
ϵ	-	voidage
Ψ_c	-	circularity
Ψ_s	-	sphericity
$\rho_{aerated}$	kg/m^3	aerated bulk density
ρ_{tapped}	kg/m^3	tapped bulk density
σ	Pa	normal stress
σ_{PSD}	µm	PSD spread in terms of standard deviation
τ	Pa	shear stress
A	m^2	area
C	-	compactness
d_{32}	µm	Sauter diameter
f	-	Heywoodfactor
Δm_i	g	mass residue
Δp	Pa	pressure drop
P	m	perimeter
ΔP_i	-	mass fraction
q_{3i}	%/µm	Frequency
S_V	1/µm	specific surface
u_0	m/s	superficial velocity
u_{mf}	m/s	minimum fluidization velocity
u^*_{mf}	m/s	weighted minimum fluidization velocity
$\dot{V}$	m^3/s	volume flow

$\bar{x}_3$	µm	mean particle size
$x_{50,3}$	µm	Median
$\bar{x}_i$	µm	average mesh size
Δx_i	µm	intervall between meshes
x_i	µm	mesh size
$x_{mode,3}$	µm	Mode

1

Introduction

1.1 Carbon dioxide - today's worst enemy?

Radiation plays an important role in establishing the climate conditions on our planet. The energy balance derived from emissions and immissions of radiation is considered to be essentially influencing the global temperature. Since CO_2 is a radiatively active species, an increase of its atmospheric concentration is regarded to alter the energy balance and hence the global temperature.

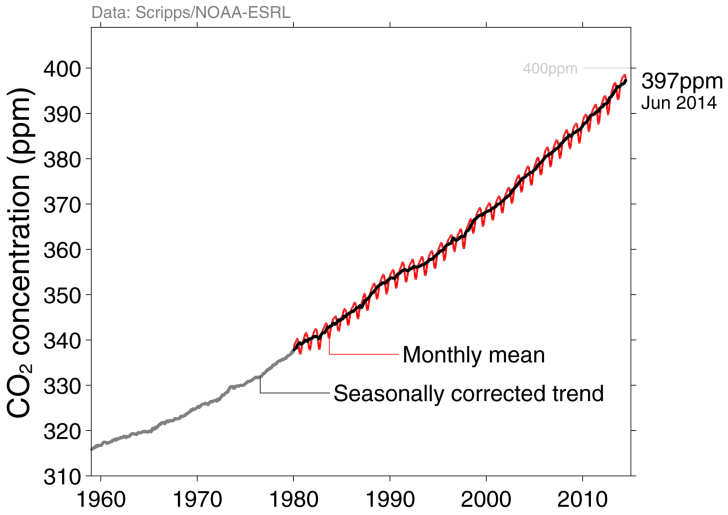

Figure 1.1: Atmospheric CO_2 concentration from 1960 to 2014 from Mauna Loa Observatory, Hawaii [1]

Figure 1.1 depicts the Keeling Curve, which is based on continuous measurements at the Mauna Loa Observatory in Hawaii. It represents the increase of CO_2 since 1958. According to this source alone in the years from 1958 until today the annual average concentration has increased from 316 ppm to around 399 ppm. [1] This is particularly alarming considering that in 800.000 years before industrialization CO_2 never rose above 300 ppm. [2] By unleashing a huge amount of carbon dioxide into the atmosphere in a very short period, humankind might have triggered a process, which will deeply influence climate conditions. This process is somehow unpredictable, but it seems that for a majority of the people the effect could be devastating. Humankind is at crossroads: either risk radical change or expressly empower a zero-carbon economy.

1.2 CCS - a strategy for mitigation

The way towards a decarbonized society is diverse and in the end only a mixture of different approaches will be successful.
Ideally fossil fuels would not be exploited and burned at all, since they are linked to many environmental hazards.
However completely replacing fossil fuels is a huge challenge and will take a lot of effort and time. Not least because there are strong actors which have monetary interest in exploiting fossil fuels as much as possible.
Hence there is the immediate need for maintaining the use of fossil fuels in a more sustainable way. By sequestrating and storing the carbon dioxide from the exhaust of large point sources, combustion of fossil fuels could be at least a CO_2 neutral process. Considering that large point sources like power plants make up for around 60 % of global CO_2 emissions, implementation of CCS seems very straightforward for mitigating climate change. [3]
CCS could even achieve more than just prolonging the lifetime of coal power plants. It could also be a way to actually reduce the amount of carbon dioxide in the atmosphere. By using biomass in combination with CCS "negative" CO_2 emissions could decrease the atmospheric concentration.
Three steps have to be considered in order to benefit from CCS. First CO_2 has to be captured from the point source. Since combustion is usually conducted with air, the main component of the exhaust is nitrogen. Only 10-15 % is the actual dry concentration of CO_2, insufficient for a reasonable storage. Oxyfuel, post- or pre-combustion technologies are established methods for sequestrating carbon dioxide. All those technologies are feasible, but come with a substantial energy penalty.
Second the carbon dioxide has to be transported to the storage. Using common pipelines this is no major obstacle.
Finally there is storage itself, most likely an underground geological formation, capable of securely storing CO_2 for centuries. Since 1996 1 Mt CO_2 is annually successfully injected from the Sleipner gas field into an aquifer in the North Sea. However much experience is still lacking and storage - at least onshore - remains a very controversial topic. [3] [4]

1.3 Chemical-Looping Combustion - a game changer?

One of the main barriers for implementing CCS is the cost factor. For power plants the capturing process is supposed to be the largest component of the overall CCS costs. [3] Decreasing this factor could be vital for realizing future projects.
Chemical-Looping Combustion enables inherent carbon dioxide separation, without additional energy intensive steps. This 2nd generation capture technology has therefore the potential to trigger a wave of CCS implementations for upcoming plants.
In contrast to most other CO_2 capturing processes, CLC does not require gas separation. In fact fuel and air are handled separately in two different active reactors. The oxygen for combustion of the fuel is conveyed from the air reactor to the fuel reactor by means of a metal oxide. The principle is depicted in Figure 1.2

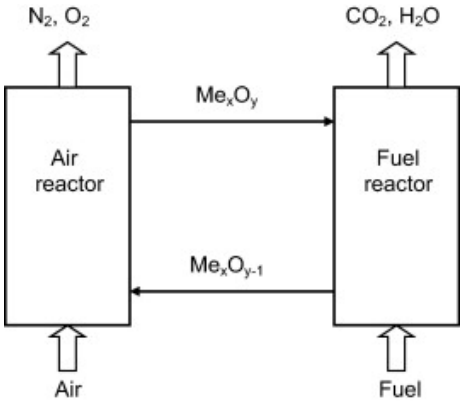

Figure 1.2: Principle of Chemical-Looping Combustion

The concept was first introduced by Lewis and Gilliland (1954) for the production of CO_2, Ishida and Jin (1997) recognized it as a potential method for applying CCS. Lyngfelt et al. presented in 2001 the first design for CLC using circulating fluidized beds and methane as fuel. [5] In the meantime CLC has been demonstrated widely with gaseous fuels. However the focus nowadays has shifted towards solid fuels, particularly because coal is still by far the most commonly used fuel in combustion power plants.
The concept of CLC with solid fuels has been realized in eleven demonstration plants ranging from 0,5 kW to 3 MW. Almost all of them use fluidized beds as basis for operation. The air reactor is built as a high velocity fluidized bed and acts as a driver for the circulation of the bed material. The bed material is essentially the metal oxide. Several different design concepts for CLC fuel reactors have been presented. The main challenge is to provide sufficient residence time for the fuel, mainly for the char. Long fuel residence time can be assured by inclusion of a carbon stripper and by highly efficient cyclone(s).
The chemical reactions concerning solid fuels are somewhat more complex, since solid fuel consists of char and volatiles. At temperatures around 970 °C volatiles are almost instantly released. The char however has to undergo steam gasification in a prior step. Gasification is way slower and takes several minutes. Operational experience indicates that especially the reaction with volatiles is limited - primarily due to insufficient contact between gas and oxygen carrier - and thus the exhaust from the fuel reactor still contains unburnt gases besides the desired CO_2. The overall process performance is measured by the amount of unconverted gases and by the fuel slip from the fuel reactor to the chimney and the air reactor. [4] [6] [7] [8] [9]

1.4 The oxygen carrier - backbone of CLC

Overall performance is largely governed by the capability of the oxygen carrier. The carrier is oxidized by the air and reduced by the fuel at temperatures near 1000 °C. In order to handle those conditions specific requirements are necessary. A high reactivity regarding both oxidation and reduction is the main criteria, which has

to be considered in the first place. It was found that transition metal oxides are most promising with respect to the reductive and oxidative thermodynamic and kinetic properties. Therefore nickel, copper, cobalt, iron and manganese oxides were treated as suitable candidates for oxygen carriers. Broad investigations have been made with several oxides, for example with Fe_2O_3/Fe_3O_4 or Mn_3O_4/MnO, and also with combined oxides, for example $(Mn_ySi_{1-y})O_x$. [10] Besides its thermodynamic nature, there are several other aspects to consider which a good carrier material should fulfill:

- High oxygen ratio: Ability to convey a high amount of oxygen per unit mass in order to decrease circulation rates.
- Capability to convert a fuel entirely to CO_2 and H_2O.
- Mechanical stability - Resistance against fragmentation.
- High melting point
- Large surface area
- Good flowability - Fluidizable, resistant to agglomeration.
- Environmentally benign, low toxic, and economically feasible.

The list of requirements is long and ambitious and the ideal carrier has still to be found. Existing investigations have been largely focused on thermodynamics and kinetics, while aspects like flowability have been covered poorly.
Natural occurring ores are providers of metal oxides in various compositions and are targeted as low cost option for oxygen carriers. Ores have been successfully used in different rigs, most prominently Ilmenite which is a common titanium-iron oxide mineral. Especially for the use with solid fuels cheap ores are highly interesting. Ash discharge and ash fouling may decrease the lifetime of the carrier severely and thus the cost factor plays an important role.
Another reasonable possibility is to use industrial agents as for example the SinFin material which is investigated in this work. The most expensive way to acquire carriers is by synthesizing a metal oxide on a supporting material. This can be done by freeze-granulation, spray drying or various other techniques. [4] [11] [8]

2

Understanding Flowability

2.1 Approach

Concerning granular systems, flowability can be defined as the ability of a powder to flow freely, in a regular and constant way. This definition seems comprehensive, though it is not said in which actual situation the powder flows freely. In fact a given particle arrangement may flow in one situation easily, but in another it needs an external stimulus.
It would be a great advancement to understand the underlying physics and thus be able to predict how a powder will behave in any given situation.
A powder consists of a huge number of individual particles. In a cubic centimeter one million spherical particles with a diameter of 100 µm can exist. Those particles interact with each other, but of course also with the surrounding environment.
There are basically two approaches on how to theoretically describe the global behavior of such a system. On the one hand the individually shaped particles are regarded and calculation of the interactions are made for every particle. Although computational methods (discrete element method) exist and computers are getting more powerful, it is still a challenge to simulate that many particles with different shapes.
On the other hand the powder can be regarded as a continuum. This has the advantage that classical continuum mechanics can be applied. Here volume elements are regarded, which are big enough that the individual particle forces can be neglected. Instead forces or stresses on the boundary areas are the matter of interest. [12]

2.2 Continuum mechanics

There are two major forces i.e. stresses which are considered in continuum mechanics. The stress acting perpendicularly to an area is the normal stress. It can originate for example from cohesion or gravitation. The stress parallel to the area is called shear stress. In bulk solids technology it is always connected to frictional effects.
This can be illustrated if one imagines a plane with a powder which gets inclined. A shear stress is transferred and the powder will remain at rest as long as shear stress becomes not less than the gravitational force.
Regarding a cylinder a bulk solid at rest is also able to transfer shear stress to the wall of a cylinder which ultimately supports the structure of the bulk material. This will result in a different pressure behavior, comparing to a newtonian fluid.

The pressure in the cylinder will not increase linearly as it is seen from a newtonian fluid, but become rather stagnant after a specific depth.
Another difference to newtonian fluids is the anisotropy of pressure or stresses. Assuming a container with infinite filling height and frictionless walls, the hydrostatic pressure acts equally in every direction, whereas in a bulk solid vertical stress exceeds horizontal stress.
In viscosity measurements of fluids a sample layer experience a varying rate of shearing strain and the shear stress is measured. Theoretically the same procedure can be applied to a bulk solid. The difference is that the response of shear stress of bulk solids is fairly independent of the rate of shearing strain. There is another parameter, which has a much bigger influence. It is the normal stress or compressive stress. [12] This coherence is depicted in figure 2.1.

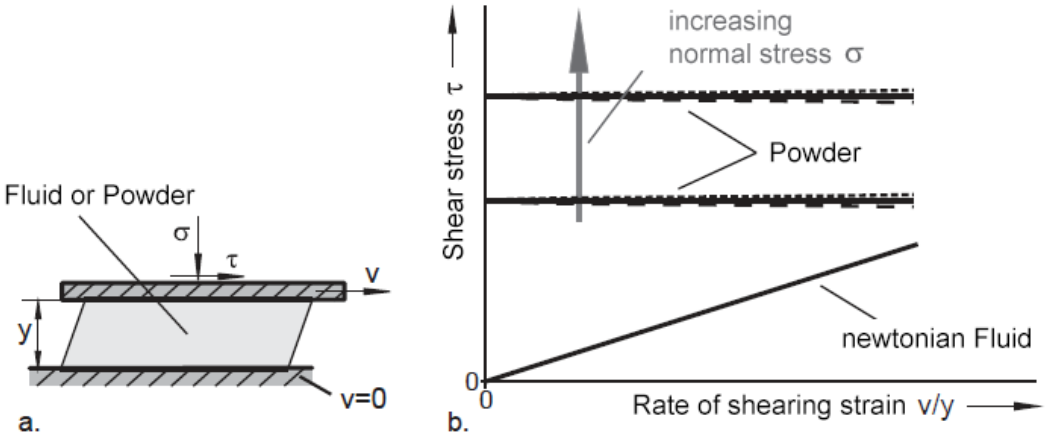

Figure 2.1: a. Schematic setup of an experimental viscosity measurement b. Stress-strain relationship for Powder and Fluid [12]

In bulk solids it is therefor common to plot shear stress versus normal stress. Investigations can be done similar to the conventional viscosity measurements, but with varying consolidation stresses. Those tests are conducted in so-called shear cell testers.

2.3 Adhesive forces

Responsible for the different behavior of bulk solids are mostly adhesive forces between the particles. The magnitude of those forces combined with the amount of external force can create completely different flow pattern. Hence a material can behave like a fluid, as seen in a fluidized bed. But on the other hand it can also be similar to a solid, if high consolidation is applied (e.g. briquetting). Adhesive forces can either lead to unsolicited phenomena, like clogging or caking but they can also be very useful for agglomeration processes or powder coating.
The most important forces are the van der Waals force, the electrostatic force and in case of moist powders liquid bridges. Van der Waals force is a collective term for forces arising from the polarity or non-polarity of molecules. They are always

existing and their intensity is dependent on particle size, distance and on chemical composition. The Lifschitz-van der Waals constant accounts for the influence of the material.
Due to different electric potentials on the particle surfaces electrostatic forces exist. The force depends on the nature of the material, if it is a conductor or an insulator, as well as on the distribution of charges.
Liquid bridges can be formed between particles if sufficient fluid of low viscosity is available. The resulting force of the liquid bridge is composed of surface tension and pressure deficit in the bridge. The latter is also referred as capillary pressure.
All adhesive forces are decreasing with increased distance between particles. The liquid bridge, if formed, is the strongest force and decreases only little. Van der Waals forces are also strong, but only at very small distances. They decrease rapidly with increasing distance. Electrostatic forces do not decrease so much, but have usually a lower magnitude in the first place.

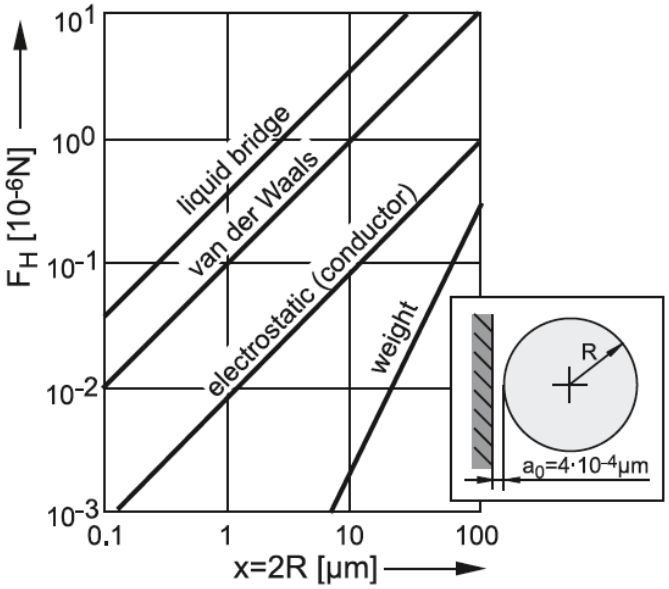

Figure 2.2: Influence of particle size x on adhesive forces
Note: Calculations which lead to figure 2.2 are highly idealistic and in reality adhesive forces are smaller, since real surfaces are rough instead of smooth.[12]

Figure 2.2 illustrates the influence of particle size on the individual adhesive forces. A spherical particle is brought near a wall under ideal conditions. Additionally to the adhesive force the weight of the particle is plotted. For small particle sizes adhesive forces clearly exceed the weight force and this explains why particles can stick to a vertical wall. Above a certain particle size weight becomes dominant, as the slope of weight (proportional to the third power of the diameter) is higher.
Concluding previous considerations smaller particles lead to an increased strength of the bulk and therefore to a decreased flowability.[13] [12]
The strength also tend to increase if the span of a particle size distribution increases, since more contact area is available.
However in this context it is noteworthy to explain the effect of flow agents, as

they are very small compared to the bulk and actually decrease the adhesive forces. Figure 2.3 shows particle arrangements with different coverage of flow agents. An

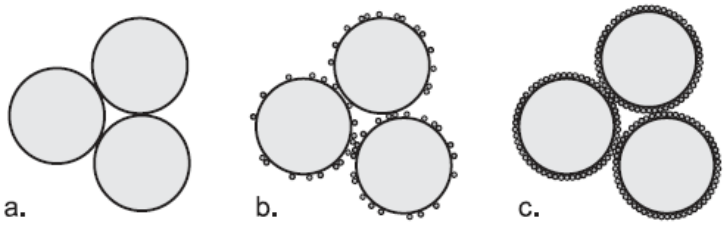

Figure 2.3: Particles covered with different amount of flow agents; a. none b. partially covered c. completely covered [12]

agent increase the distance between the grains and thus decrease the forces between them. Usually only a small percentage (up to 1 % by weight) of agent is needed to build up the effect, shown in figure 2.3 b. Adding more agent will lead to total coverage (Figure 2.3 c.) and will not lead to further improvement, but more likely has an opposing effect, as contact areas increase again. The influence of the size

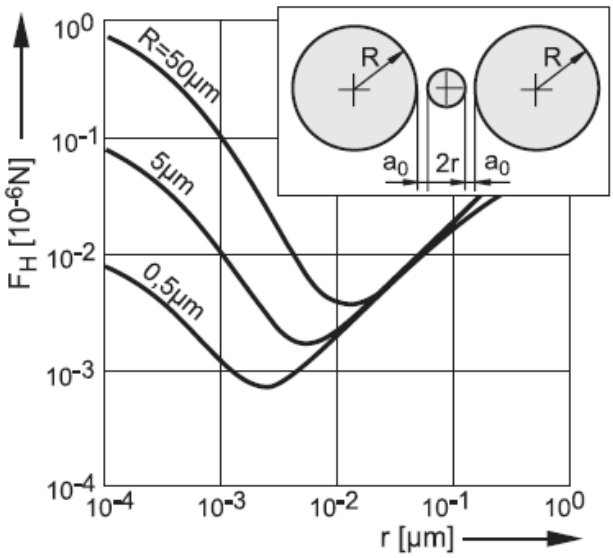

Figure 2.4: Influence of agent radius r on the adhesive forces between two spherical particles [12]

of the agent is depicted in figure 2.4. Ranging from some nanometers to less than a micron, flow agents have to be very small compared to the bulk in order to be effective. The reason is the that the agent itself also possess adhesive forces, which have to be limited.
Particles of such small size tend to agglomerate, which makes an even distribution of agents difficult. Also it is possible that particles of the flow agent fill grain pores and so smoothen the actual surface. Attrition and fragmentation during CLC operation can produce very fine particles. Those particles can act as a flow agent, but if the

concentration exceeds a certain amount, negative effects on flowability are more likely.
The average distance between particles might not only be influenced by flow agents, but also by the shape of the particles itself. If particles are roughly shaped, contact area should be smaller and so should adhesive forces. This improvement of flowability, due to irregular shape can only be seen for fine cohesive powders. More coarse particle systems will instead benefit from regular spherical shaped particles.
Furthermore water adsorption layers can play a significant role. If granular material is exposed in a humid environment, adsorption layers can build up way below a relative humidity of 60 %. Adsorption can vary from monolayered to multilayered. Exceeding relative humidities of 60 % can lead to capillary condensation, as a result of reduced saturation vapor pressure over particle pores. The effect of adsorption layers is complex, it may increase or decrease van der Waals forces, depending on material properties. If liquid bridges can be formed due to capillary condensation, adhesive forces can be completely dominated by the liquid bridges. [14] [12]
Another phenomenon which has an influence on adhesive forces is the time consolidation. Bulk solids which remain at rest for some time may experience an increase in cohesion. This can happen because of

- visco-plastic or plastic deformation of particles and consequently increased contact areas.
- creation of solid bridges from processes like evaporation of solvents or sintering.
- chemical or biological reactions.

Last but not least it is important to consider that bulk solids possess a stress history. External applied forces can induce large local stresses within the bulk, since the contact points are small. This ultimately leads to plastic deformation which again increases the contact areas and thus the adhesive properties. Especially fine, cohesive material can be manipulated by compression in such way that it will stick profoundly together. Tabletting exploits this very phenomenon. [12]

3
Investigating flowability

3.1 Rationale

There had been unresolved issues at the CLC test rigs at Chalmers during operation. Particularly the following problems occured:

- Poor flow through particle seals
- Poor flow from hopper during refilling of carrier material into the reactor system
- Poor fuel conversion compared to experiments in lab reactor
- Agglomeration
- Fuel slip at unexpected places, possibly due to slugging

These problems raised the question, if or to what extent physical properties of the carriers are responsible for such behavior. Since the granular oxygen carriers are constantly moved in the reactors, their flowability was considered crucial to investigate.
Besides theoretical considerations, an experimental investigation was launched in order to gain more insight into the flowability of carrier material. Ideally experiments would have been conducted in cold and hot conditions, due to the fact that the actual operation takes place at about 800 - 1000 °C. However performing experiments at high temperatures might not be possible at all, since sintering or agglomeration could occur and alter the results. In order to prevent this in the actual CLC process, particles are kept fluidized all the time. Experiments at elevated temperatures would also require much more elaborate equipment and safety matters. Hence experiments were conducted only at ambient conditions. The effect of high temperature on flowability properties is not clearly established from literature, but investigations from Tomasetta indicate no or a only a weak deterioration. [15]
As addressed in the previous chapter flowability is a complex mechanism and a lot of parameters can play a role. Among them are certainly grain size distribution and particle shape. These parameters are important for the magnitude of adhesive forces. In this work they are investigated by sieving and microscopy.
In the further process of choosing experiments to conduct, several possibilities came up. There is a rather sophisticated way of performing flowability investigations using the shear cell testers, addressed in chapter 2.2. This method is supposed to

deliver reproducible results and evaluates samples under different circumstances i.e. consolidation. The drawback is that expensive and complex equipment has to be handled and more important that results are not conclusive for free-flowing powders. [12]
Since from preliminary examinations the considered oxygen carriers were supposed to be free-flowing, the use of shear cell testers was not seen as necessary. Another approach is to perform different small experiments and compare the outcome. Additionally a reference powder was introduced, which was considered as a well flowing material.
The experiments should cover different situations and environments in order to get a meaningful assessment. The flow through a funnel, the angle of repose and the Hausner ratio are classic tests in powder technology. They address static as well as dynamic behavior. To embrace the fact that the actual state of operation of the carriers is in fluidization, the minimum fluidization velocity was experimentally investigated and compared with calculated values.
In the following the different experiments are presented in detail, but first the investigated carriers are introduced.

3.2 Oxygen carrier selection

The investigation aimed to compare different oxygen carriers, which are suitable for CLC. Carrier materials which had been used in CLC with solid fuels, as well as fresh material were included in the selection process. The idea was to take a fresh and a used sample from each species, so they can be directly compared. Due to limited availability, this could not be fully established. The selection included naturally occurring ores, mixtures of ores, one synthetic material and as a reference sand. The ores can principally be distinguished between iron ores and manganese ores.
Table 3.1 lists the investigated materials. In the column "Used" is noted, in which unit the carrier has been operated and where it has been extracted. Detailed informations about the elementary composition of the carriers and descriptions of the different test rigs at Chalmers are given elsewhere. Referring to the materials in this work will be handled as following: [Name:Condition]. For example fresh Mesa: [Mesa:F], or used Ilmenite from the 100 kW Filter: [Ilmenite:100kW,Filter].
One sample is not listed in Table 3.1, since it is a mixture between Ilmenite and Buritirama. It contains 90 % Ilmenite and 10 % Buritirama. It was tested in used condition, extracted from the 100 kW fuel reactor: [IlmBuri:100kW].
Besides using the materials as they were, samples have been sieved in order to get rid of very fine and very large size fractions. Those fractions were suspected to affect the overall material behavior significantly. The sieved samples have a size range of 90 µm to 300 µm. They are given the nomenclature: [Name:Condition:**S**].
For further investigating particle mixtures with a high fraction of fines some artificial blends were created. The mixtures are based on ordinary [Sand:F] and Mangagran fines were added in different proportions. Mangagran is a manganese ore supplied by Sibelco and the fines are basically the "waste" from wet sieving. Their particle diameter is mostly below 45 µm, but suspected to be considerably smaller, since

Table 3.1: Investigated oxygen carriers

Name	**Main component**	**Origin**	**Fresh**	**Used**
Sand	SiO_2	*Baskarpsand AB, Sweden*	x	-
Ilmenite	Fe_2TiO_5/TiO_2	ore for steel, paint industry *Titania A/S; Norway*	x	10kW, FR & 100kW Filter
Tierga	Fe_2O_3	pigment for paint industry *Promindsa; Zaragoza, Spain*	x	100 kW, FR & Fines
Mesa	Mn_3O_4	ore for steel industry *Australia*	x	10 kW, FR
SinFin	Mn_3O_4	agent in steel processing *China*	x	100 kW, LS2
Buritirama	Mn_3O_4	ore for steel industry *Min. Buritirama S.A.; Brazil*	x	-
C14	$CaMn_{0.875}Mg_{0.1215}O_3$-d	*VITO, Belgium*	x	10 kW gas

they tend to heavily agglomerate. The blends are refered as [Blend:XX%]. Blends with 5 %, 10 %, 15 % and 20 % of fines were prepared.

3.3 Experimental work

3.3.1 Sieving

3.3.1.1 Background

A granular system consists usually of particles with different sizes. Sieving is a well known way to get access to the size distribution. It is a useful technique, as particles are classified only according to their size. Properties concerning density or surface do not alter the results gained from sieve analysis. The principle of a sieve analysis is to obtain mass fractions of a sample in specific size intervals. Those intervals are given by the applied sieve aperture range. Mesh sizes for analysis are standardized and available in a wide range from 5 µm to 125 mm. [16, 17]

3.3.1.2 Setup & Procedure

The sieving of the powders was carried out in a specific way, which grants accurate results and reproducibility. Using samples with a initial mass of 175 g was found suitable, as it is sufficient to minimize weighing errors, but it was still possible to homogeneously penetrate the mesh. The sieving process was divided in two steps. First the sample was wet sieved on the smallest available mesh (45 µm). This was necessary to get rid of the very fine material, which might have clogged the sieves. After the sample was dried again, dry sieving was conducted. At most eight sieves with apertures ranging from 90 µm to 355 µm were utilized. The Octagon sieve shaker from Endecotts Ltd. was set to an amplitude of 5. The sieving time was 20 minutes. In order to perform the analysis the sieves were weighed before and after the process.

3.3.1.3 Analysis

Table 3.2 shows an example of how the data obtained from sieving can be depicted and analyzed. The mass residue is the main outcome from the sieving experiment. It describes the mass which remained on the lower sieve of the according size range. With that value it is straightforward to calculate the mass fraction and the frequency. The frequency incorporates the interval width, which varies from 25 to 50 µm, simply by dividing the mass fraction by the interval. The frequency curve is depicted in Figure 3.1. From the curve it is easy to see which fraction is the most common. In this case it is the fraction from 125 to 150 µm. In the middle of this range the Mode $x_{mode,3}$[1] of the distribution is found. The graph also visualizes the difference between frequency and mass fraction. The mass fraction would contraindicate that particles in the range of 150 to 180 µm are most common. Another possibility to visualize the data is to plot cumulative distribution curves, as seen in Figure 3.2. The undersize cumulative distribution (Passage) is the accumulated mass fraction which passes the respective size range, the oversize curve (Residue) is just the opposite. The crossing

[1]Note: The nomenclature concerning particle size involves 3 because data is taken from volume/mass based measurements. In case of measured particle quantity it would be 1

at P(x)=R(x)= 0,5 is the median $x_{50,3}$ of the distribution. It is at around 152 µm. [16]

Table 3.2: Obtained data from sieving [C14:F]

Mesh x_i µm	**Interval** Δx_i µm	**Mass residue** Δm_i g	**Mass fraction** $\Delta P_i = \frac{\Delta m_i}{\sum m}$ %	**Frequency** $q_{3,i} = \frac{\Delta P_i}{\Delta x_i}$ %/µm	**Passage** $P_j = \sum_1^J \Delta P_i$ -
0 to 45	45	0,7	0,4	0,009	0
45 to 90	45	1,9	1,1	0,024	0,004
90 to 125	35	30,2	17,3	0,493	0,015
125 to 150	25	52,3	29,9	1,195	0,188
150 to 180	30	60,1	34,3	1,145	0,486
180 to 212	32	29,1	16,6	0,520	0,83
212 to 250	38	1	0,6	0,015	0,996
250 to 300	50	0,2	0,1	0,002	1
$\sum$		175,5	100		

In order to compare different size distributions it is useful to have a single value which represents the sample. There are many different characteristic values, the Mode and Median have already been mentioned.
For the weighted average all present particle sizes are contributing, regarding their mass fraction in the sample. The calculation for discrete values is shown in Equation 3.1. Table 3.3 provides the results of the calculation for the regarded example.

$$\bar{x}_3 = \sum_{i=1}^{n} \bar{x}_i \frac{\Delta m_i}{\sum m} \tag{3.1}$$

In many applications the surface area of the particles plays an important role. To address this the specific surface can be determined. Generally spoken the specific surface is defined as particle surface divided by its volume or mass. The volume based specific surface can be found by applying Equation 3.2. f is the Heywoodfactor, which attributes for a non-spherical shape. In case of a sphere f equals 1. [16]

$$S_V = \frac{6 \cdot f}{x} \tag{3.2}$$

For a particle population the specific surface can be easily calculated under the assumptions that f is constant and the density is independent from particle size. [16]

$$S_V = 6 \cdot f \cdot \sum_{i=1}^{n} \frac{\Delta P_i}{\bar{x}_i} \tag{3.3}$$

With Equation 3.3 and the values from Table 3.3 the specific surface can be stated as 0,053 µm $^{-1}$. An average Heywoodfactor of 1,25 was assumed for all ores (correlates to a sphericity of 0,8). C14 is considered spherical. In close relation to the specific surface is Sauter diameter d_{32}. It is defined in Equation 3.4.

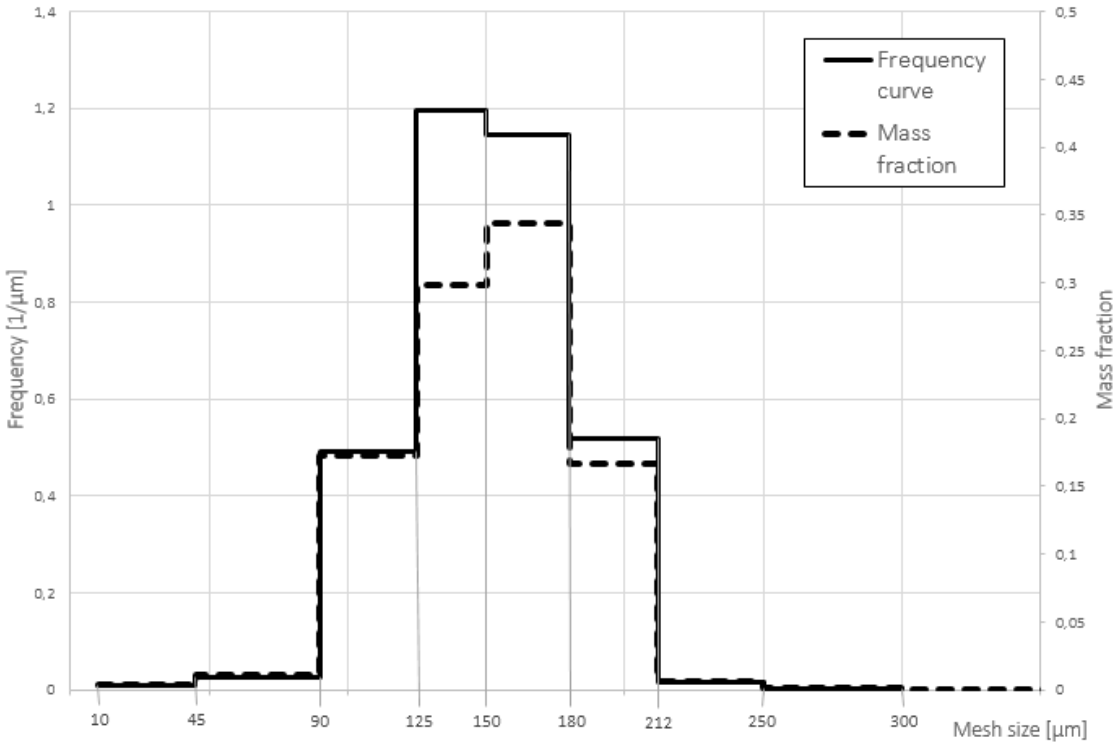

Figure 3.1: Mass fraction and frequency curve of sieving analysis of [C14:F]

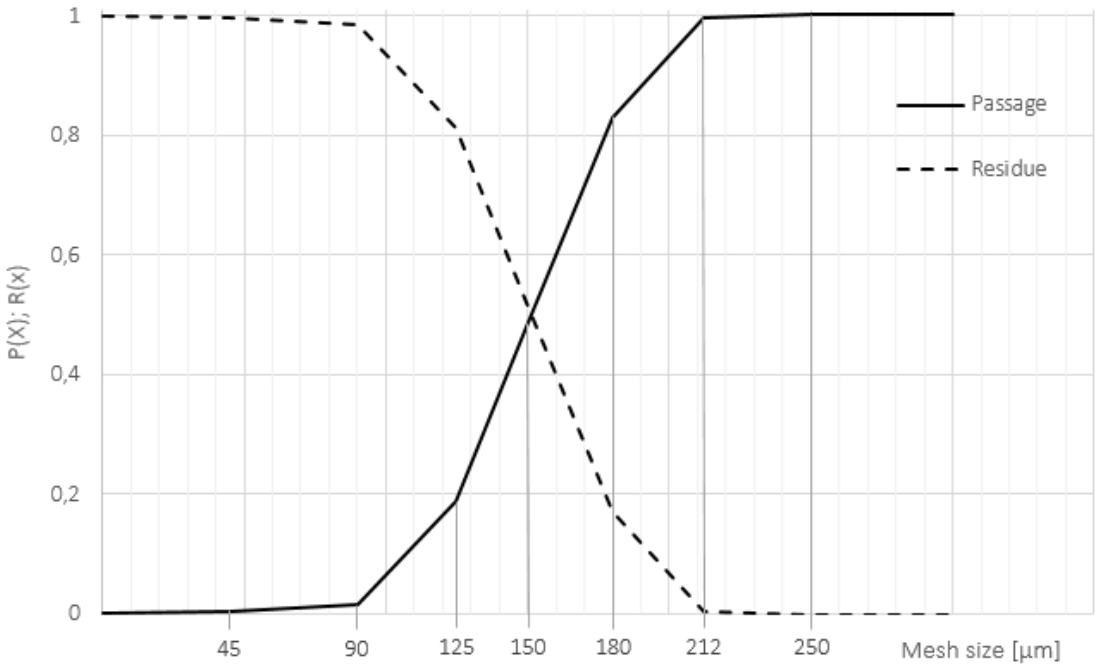

Figure 3.2: Cumulative distribution curves of sieving analysis of [C14:F]

$$d_{32} = \frac{6}{S_V} \tag{3.4}$$

It depicts the specific surface of the particle population as a mean size of a sphere. In the example of [C14:F] the Sauter diameter is 141,3 µm.

Table 3.3: Obtained data from sieving [C14:F]

Mesh	**Average size**	**Mass fraction**		
x_i	$\bar{x}_i$	$\Delta P_i = \frac{\Delta m_i}{\sum m}$	$\bar{x}_i \cdot \Delta P_i$	$\frac{\Delta P_i}{\bar{x}_i}$
µm	µm	%	µm	μm^{-1}
0 to 45	22,5	0,4	0,09	1,78e-04
45 to 90	67,5	1,1	0,73	1,61e-04
90 to 125	107,5	17,3	18,55	1,61e-03
125 to 150	137,5	29,9	41,09	2,17e-03
150 to 180	165	34,3	56,67	2,08e-03
180 to 212	196	16,6	32,59	8,48e-04
212 to 250	231	0,6	1,32	2,47e-05
250 to 300	275	0,1	0,31	4,16e-06
$\sum$			151,36	7,08e-03

Recapitulating the different characteristic values:

Median $x_{50,3} = 152$ µm

Mode $x_{mode,3} = 137,5$ µm

Mean $\bar{x}_3 = 151,36$ µm

Sauter $d_{32} = 141,3$ µm

These values do not deliver any statement about the spread of the distribution. To address this loss of information, it is common to compute another value. For this purpose also several approaches are common within particle science. For example there is the Span, which is given in equation 3.5. D_{90} and D_{10}, as well as the Median $x_{50,3} = D_{50}$ can be read from the undersize cumulative distribution curve 3.2. [18] In the example of [C14:F] the Span would be 0,57.

$$Span = \frac{D_{90} - D_{10}}{D_{50}} \tag{3.5}$$

However the most common way to characterize the sorting, is to evaluate the standard deviation σ_{PSD}. Assuming a Gaussian distribution, 68 % of the particles are within the Mean $\pm$ σ_{PSD} and 95 % lie within a range of 2 σ_{PSD}. The computation of the standard deviation is shown in equation 3.6 [18]

$$\sigma_{PSD} = \sqrt{\sum_{i=1}^{n} \Delta P_i \cdot (\bar{x}_i - \bar{x}_3)^2} \tag{3.6}$$

The standard deviation for [C14:F] is $\sigma_{PSD} = 31,3$ µm.
Because a Normal distribution is assumed, the standard deviation is not a good indicator for the assessment of Fines. Since they are supposed to play an important role in terms of flowability, the mass ratio of particles below 45 µm is separately given.
The Median and the Mean weighted values were quite close throughout most analyzed particle distributions. The Mode value was given less attention, because of it's limited significance. Therefore the Mean, the Sauter diameter and the standard deviation were chosen in order to compare the different oxygen carriers in terms of their size distribution.

3.3.1.4 Results

Particle size results for material, which was available in fresh and used condition, are given in Figure 3.3. From the graph Mean diameter, Sauter diameter, standard deviation and content of fines below 45 µm can be read. Note that the error bar is in this case not a real error bar, but it depicts the spread of the distribution in terms of the standard deviation. More detailed values for all investigated materials can be found in the appendix (Table A.1 and A.2).

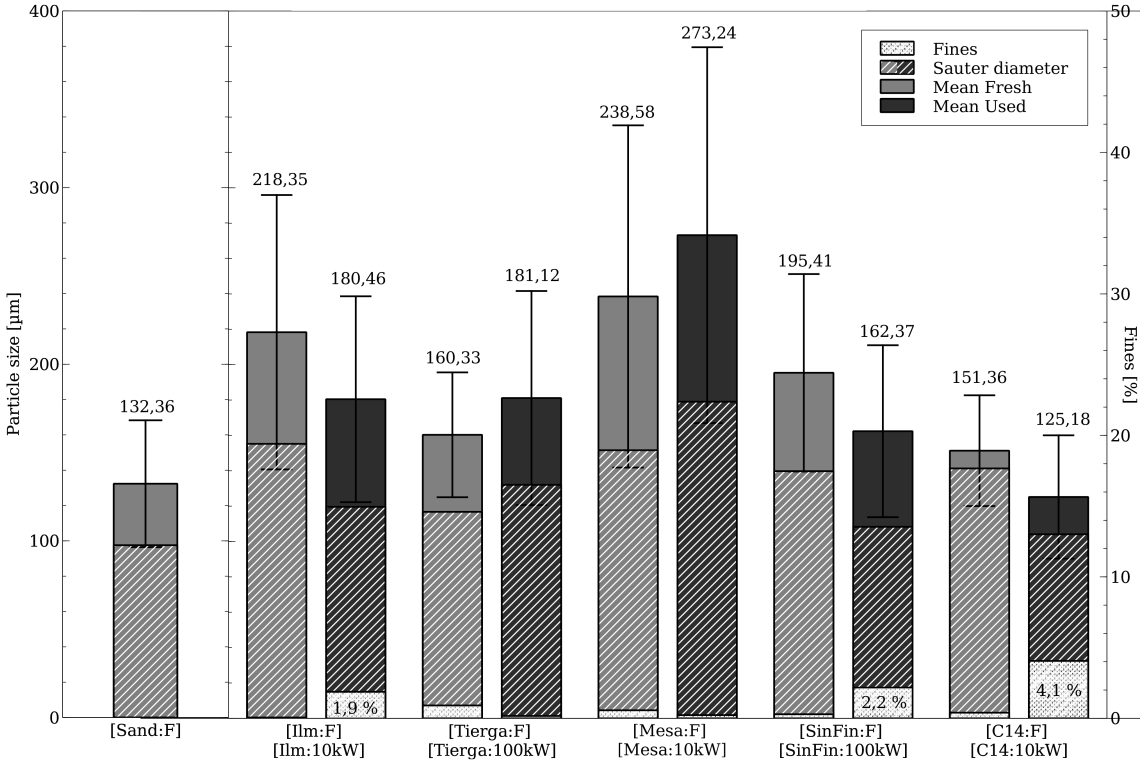

Figure 3.3: Results from sieving analysis
Note: The values above the bar ends state the Mean $\bar{x}_3$

Most notably here is the varying effect of operation, seen in the difference between the fresh and used state. There are carriers, which produce very fine material during operation. This is for example Ilmenite, Sinfin and C14. Those used materials were perceptible dusty. Contrary materials are Tierga and Mesa, which rather increase

their particle size. The increase of Tierga might however arise from issues during its operation, which made it necessary to add larger particles over time.
Mesa has clearly the largest particles and also the spread is comparable broad. Most of the investigated particles however are pretty close in respect to Mean diameter, in a range from roughly 150 µm to 200 µm. Sauter diameters are smaller, ranging approximately between 100 and 150 µm.
The broadness of the distributions varies significantly. Narrow distributions are for example seen at [Tierga:F], while [Ilm:F] has twice the spread.

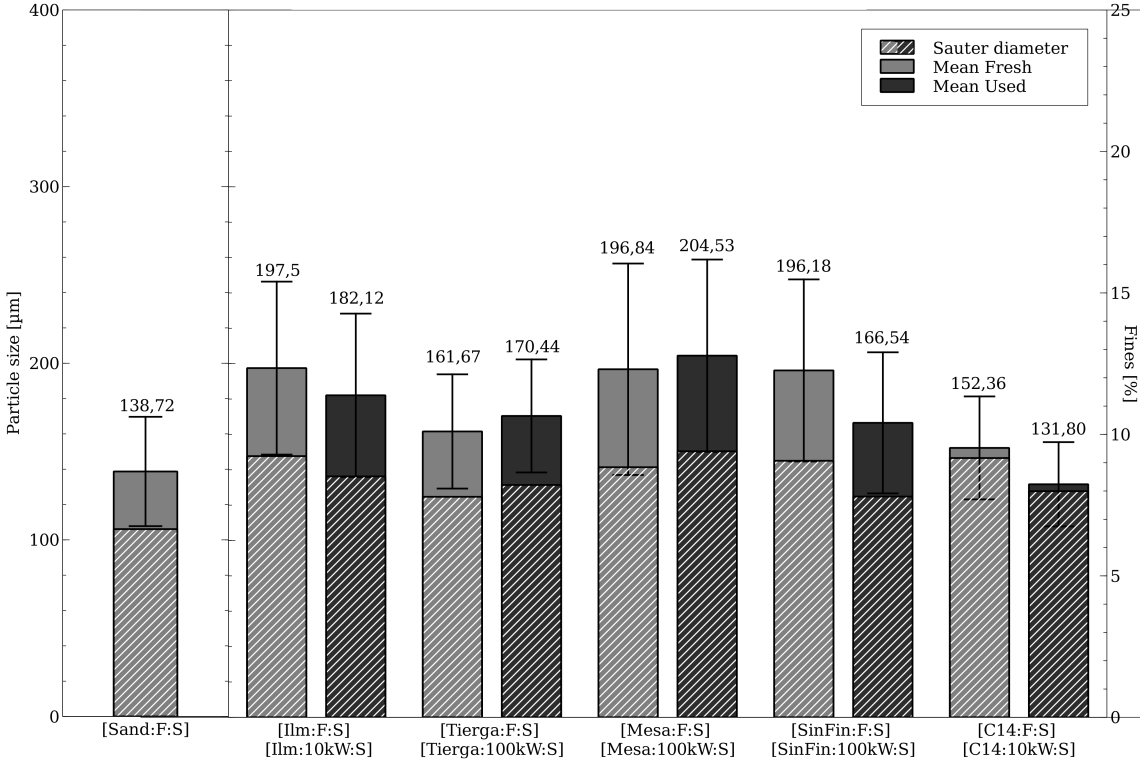

Figure 3.4: Grain size after the sieving process
Note: The values above the bar ends state the Mean $\bar{x}_3$

As outlined in Chapter 3.2 samples have been prepared in a fraction between 90 and 300 µm. The respective diameters are depicted in Figure 3.4. Obviously fines are gone and overall PSDs are harmonized. Otherwise it resembles still Figure 3.3.

3.3.2 Microscopy

3.3.2.1 Background

Particles in a collective vary not only in size but also in terms of their shape. Contrary to the size distribution, the shape distribution of a particle population can not be measured in a satisfying way. It is common just to visually examine microscope pictures in qualitative manner. Nevertheless there are definitions for shape factors, which are widely accepted. Wadell (1932) defined the Sphericity as a ratio between the surface of a sphere to the surface of the given particle. It is important that the sphere has the same volume as the investigated particle. The Sphericity takes values in the range of 0 to 1, as the surface of a sphere is the smallest possible at a given volume. [19]

$$\Psi_s = \frac{S_{sphere}}{S_{particle}} \tag{3.7}$$

Similar to Sphericity it is possible to define characteristic values in two dimensions. The analogue to Sphericity would be the circularity, which is defined as the ratio of the perimeter of an identical projection surface of a circle to the given perimeter of the particle. [19]

$$\Psi_c = \frac{P_{circle}}{P_{particle}} \tag{3.8}$$

Another method is to look at the ratio of the area of the particle projection to the area of a circle with the same perimeter. This is called Compactness.

$$C = \frac{A_{particle}}{A_{circle}} \tag{3.9}$$

3.3.2.2 Setup & Procedure

Using a light microscope, several pictures with different magnifications were taken. The microscope is a Magnus HD Prestige from Tagarno AS. Besides the qualitative observations, image analysis was used to determine a shape factor. The compactness was evaluated with the image analysis software JMicroVision v1.2.7. Therefore about 100 particles per species were extracted using a threshold technique and their circumference was smoothed until a reasonable result was visible. Thresholding was applied on all of the three RGB channels.

3.3.2.3 Analysis

Figure 3.5 shows the analysis of fresh Tierga. The particle outline is marked. The color code from red to yellow reflects the level of compactness (yellow outline = high compactness). For the selected particle image analysis delivers an area $A_{particle}$ = 1117 px^2 and a perimeter $P_{particle}$ = 128,03 px. With that values the Compactness can be computed as seen in Equation 3.10

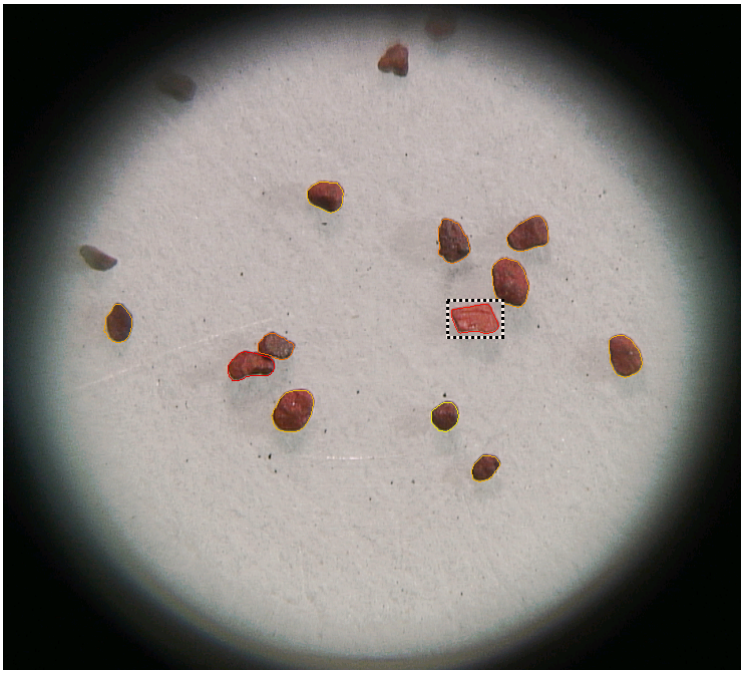

Figure 3.5: Image analysis using JMicroVision

$$C = \frac{A_{particle}}{A_{circle}} = \frac{A_{particle}}{P_{particle}^2 \cdot 1/4 \cdot \pi^{-1}} = 0{,}856 \tag{3.10}$$

Whereas Circularity would be 0,925.

$$\Psi_c = \frac{P_{circle}}{P_{particle}} = \frac{\pi \cdot d_c}{P_{particle}} = \frac{\pi \cdot \sqrt{A_{particle} \cdot 4 \cdot \pi^{-1}}}{P_{particle}} = 0{,}925 \tag{3.11}$$

3.3.2.4 Results

In order to give a good visual close-up of the particles seen from light microscopy, several pictures of different focal length have to be stacked (DFF). Figure 3.6 shows some examples of various carriers. The appearance did not change much from fresh to used condition, with the exception of the Tierga ore. There is a clear color change visible. (See figure 3.6 b. and c.)

The produced fines from attrition can be seen in figure 3.6 e, where the background is dotted. From such pictures the size of the fines can be roughly estimated. In this case fines are in the range of up to a few microns.

In Figure 3.7 compactness measurement results from image analysis are plotted. The black shape is an example of the respective compactness value.

Generally all investigated particles showed a quite high degree of compactness or circularity. Though there were differences between the carriers clearly visible and this was confirmed by the image analysis. The carrier with the lowest degree of compactness is [Mesa:10kW] and its fresh counterpart. Deducing from the images,

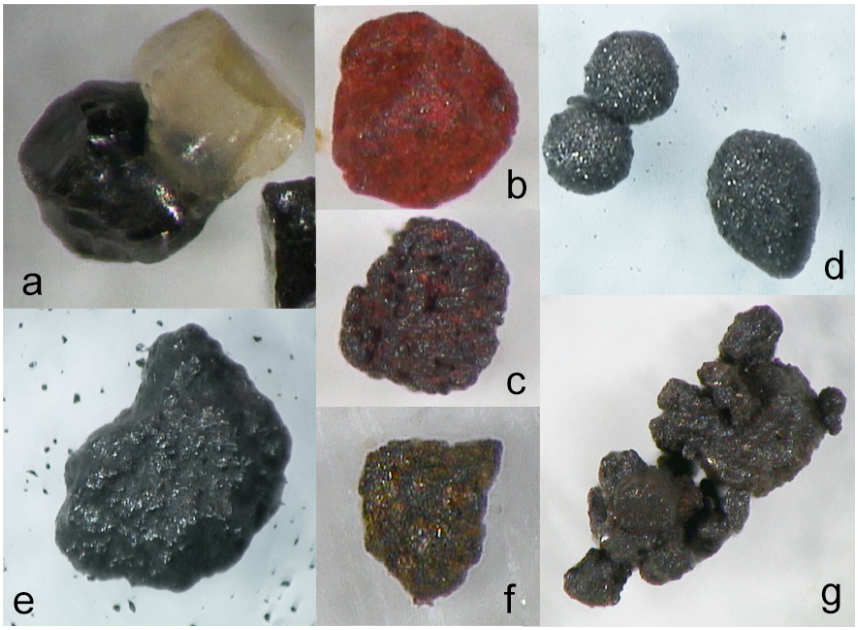

Figure 3.6: Particle images from light microscopy using DFF
a. [Ilm:F] (∼ 200 µm) b. [Tierga:F] (∼ 160 µm) c. [Tierga:100kW] (∼ 180 µm)
d. [C14:F] (∼ 125 µm) e. [SinFin:100kW] (∼ 160 µm) f. [Buri:F] (∼ 150 µm)
g. [Mesa:F] (∼ 240 µm) Note: Images are not in scale

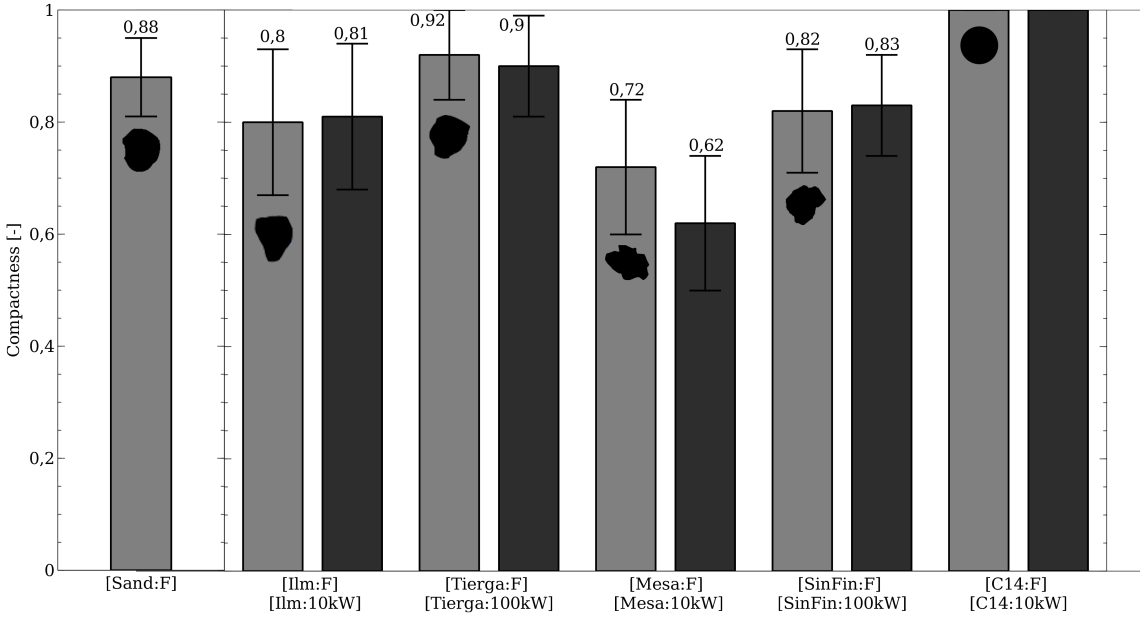

Figure 3.7: Compactness - values derived from around 100 particles per material

Mesa has experienced some kind of agglomeration. This is seen in fresh, as well as in used state. This ongoing agglomeration at elevated temperatures could also explain the difference between fresh and used state.

The other remarkable compactness shows C14. As this material is synthesized by spray-drying, it is very spherical. Thus compactness was assumed to be 1 and a deeper image analysis was not conducted.

There was no significant change in terms of shape between fresh and used state visible. This is also seen from compactness analysis. Missing in Figure 3.7 are values for [Buri:F] and [IlmBuri:100kW]. Both have the same compactness of 0,83.

It is not simply possible to derive Sphericity from 2d considerations. This is especially true for agglomerated particles like Mesa. However for the other particles it enables you to give better estimates on a solid basis.

3.3.3 Hausner Ratio

3.3.3.1 Background

The bulk density of a granular material is defined as its mass divided by the volume it occupies. In comparison to the true particle density, bulk density includes the space between the particles as well as the voids within the grains. The bulk density can change significantly because the packing varies due to different states of compaction and consolidation. [20]

These different conditions can be used for the determination of the compressibility of a material. [21] The Hausner ratio is one possible way to address the compressibility. It describes the ratio between two bulk densities. First the aerated bulk density, which represents a condition where the powder is loosely packed. This is achieved by ”allowing the dispersed powder to settle in a container under the influence of gravity” [20]. And second the tapped density, where tapping rearranges the particles to achieve a state of compaction and dense packing. Both states of packing are random, which means there is no long-range order like in a crystal structure.

Several authors relate the Hausner Ratio with the cohesiveness of the material. If structural forces are strong, the powder will resist collapse and initially occupy a greater volume. A well flowing granular material will on the other hand end up in a dense packing, which is difficult to further compress. Hence a larger difference between the two densities, i.e. an increased Hausner ratio, is supposed to represent an increase in cohesiveness of the particular collection. [20]

3.3.3.2 Setup & Procedure

First samples of about 140 g were carefully weighed. All volume measurements were conducted, using a 100 ml measuring cylinder. The pouring process followed the procedure described in Chapter 3.3.4.2 and was conducted in the same arrangement. From this initial pouring, the aerated bulk volume was determined.

Tapped volume was not obtained by tapping in a classical way, but by putting the cylinder on the sieve shaker (see chapter 3.3.1.2). Four different amplitudes were successively applied, in order to vary the tapping process and to get results from different stress levels. For the highest amplitude the cylinder had to be pressed gently on the sieve shaker in order to maintain its position. This measurement was also the basis to derive the tapped density.

3.3.3.3 Analysis

Aerated and tapped bulk densities were simply calculated by equation 3.12 and respectively 3.13.

$$\rho_{aerated} = \frac{V_{aerated}}{M} \tag{3.12}$$

$$\rho_{tapped} = \frac{V_{tapped}}{M} \tag{3.13}$$

The Hausner ratio is the quotient between those two densities:

$$H_r = \frac{\rho_{tapped}}{\rho_{aerated}} \tag{3.14}$$

There are references in literature which suggest thresholds for the Hausner ratio. For example materials which have a $H_r \leq 1,25$ are considered by Hausner as sandy or granular with good flowability. However bulk density measurements are quite sensitive to the pouring technique as well as the tapping technique, so this thresholds should be treated cautiously. [21]

3.3.3.4 Results

Figure 3.8 and Figure 3.9 show the results for the tapped density, attained from tapping with the highest sieve shaker amplitude. The amplitude is in that case around 2,4 mm. Sieving time was 30 seconds, which corresponds to 1500 vibrations per minute (50 Hz). Density varies within the different materials and for some of them it even varies between fresh and used state. This could be a sign of increasing or decreasing internal porosity or of changes in chemical composition. This is for example very distinctly seen in Ilmenite, which has a difference between used and fresh state of almost 20 %. The very small differences between unsieved and sieved condition suggest that particle size distribution has a very limited influence on tapped density. The fact that between [Tierga:F] and [Tierga:Fines] is only a difference of 3 % supports this assumption.

With further inclusion of the aerated bulk densities, Hausner Ratios can be calculated as described before. Figure 3.10 and 3.11 depicts the Hausner Ratios for either non-sieved and sieved samples.

The lines between the markers are only drawn to better visualize the group affiliation. Obviously the Hausner Ratio increases with increasing applied amplitude i.e. stress level. Through the vibrations a denser packing can be achieved. Rearrangement occurs differently for the investigated materials. Tierga for example shows a huge

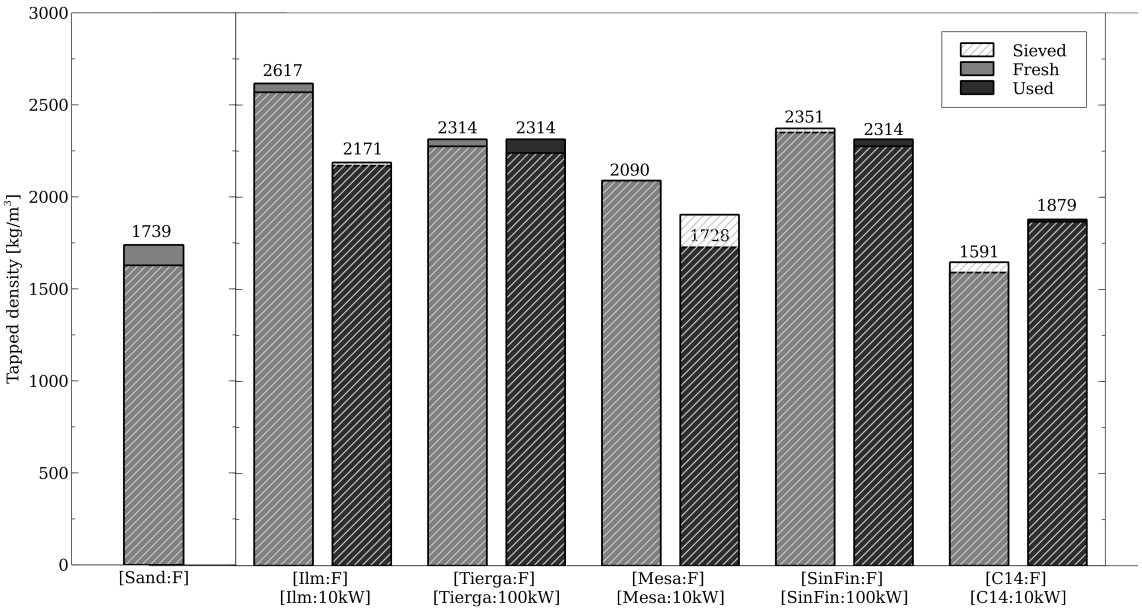

Figure 3.8: Tapped density of fresh and used carriers

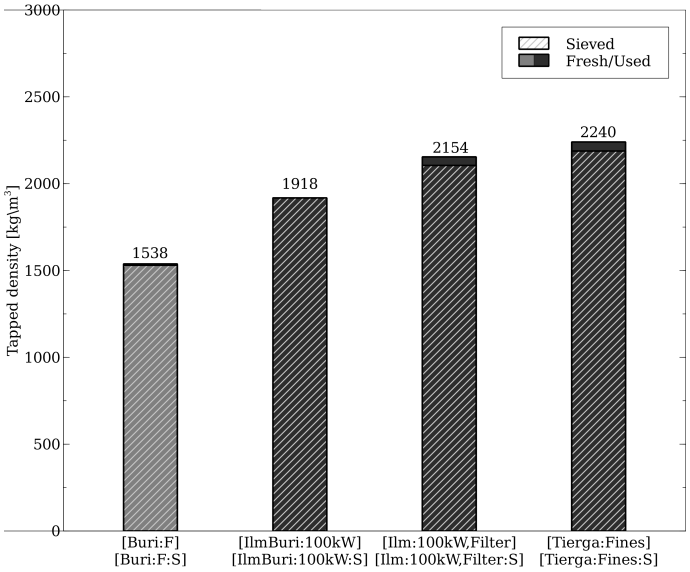

Figure 3.9: Tapped density of remaining carriers

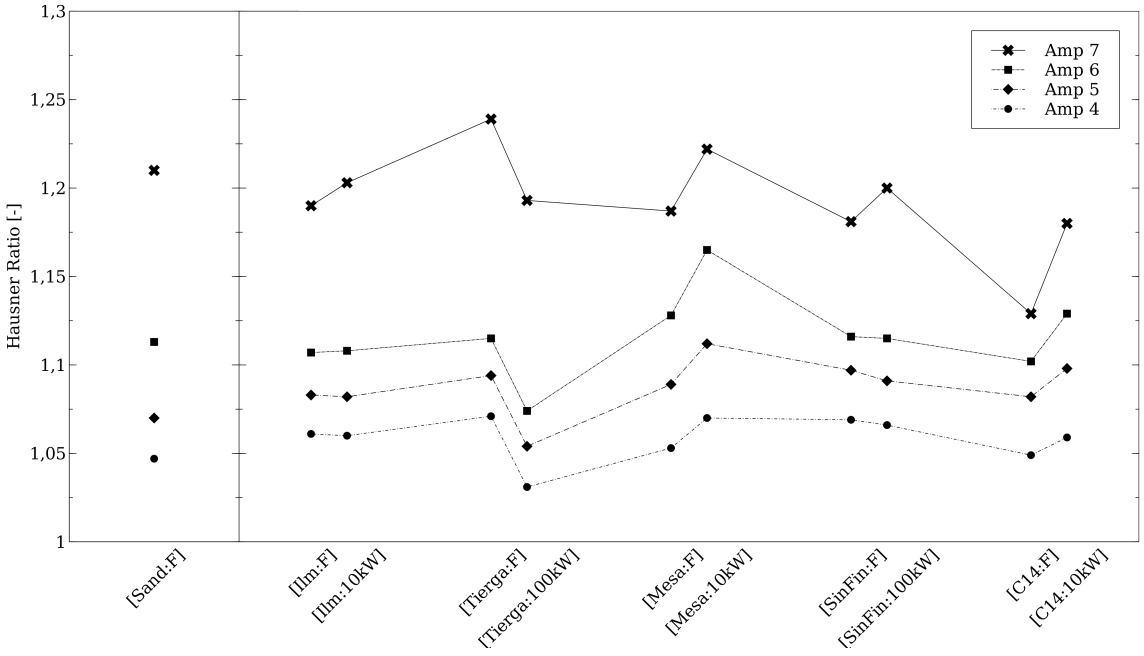

Figure 3.10: Hausner Ratio of non-sieved material

gap between amplitude 6 and 7, while before packing only changed marginally. This could be sign for initially strong interparticle forces, which first have to be overcome. This stands in contrast to Mesa and C14 which increase is much more linear.

All samples show the trend of an increasing Hausner Ratio from fresh to used state. Tierga can probably not be taken into account due to the ill-matched samples. The difference gets more distinct when higher amplitudes are applied. For Ilmenite or SinFin it is initially not seen at all, only the last amplitude reveals that there is some difference. The fact the HR increases could be originated due to the fact that those carriers (except Mesa) decrease their particle size and also produce some fines. Those smaller particles tend to have stronger interparticle forces, resulting in higher values of Hausner Ratio.

Regarding the overall picture, the Hausner Ratios of the carriers are not that far away from each other. In fact most of them are around 1.2, which is regarded unproblematic in terms of flowability.

The graph of the sieved materials is quite similar to the one above, but again harmonized. Extreme values are leveled out. The difference between the carriers becomes small, almost insignificant.

In figure 3.12 the remaining carriers are plotted, sieved and nonsieved. One aspect is striking. Despite the large amount of fines in the nonsieved [Buri:F] and [Ilm:100kW,Filter] (about 8 %), the Hausner Ratio seems not affected at all. This is a contradiction to the assumption, that fine particle increase HR.

Another picture emerges, if the blends are taken into account. Figure 3.13a conjectures again an increase of HR with increasing content of Fines.

Figure 3.13b opposes finally used SinFin and the same SinFin, but sieved to a

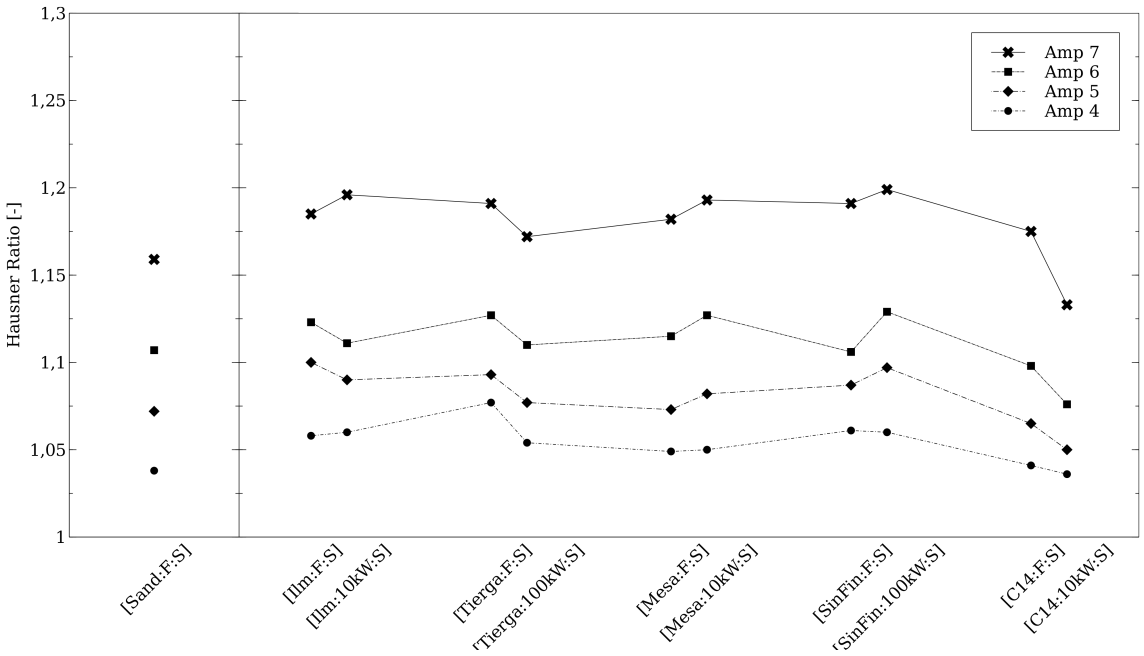

Figure 3.11: Hausner Ratio of sieved material

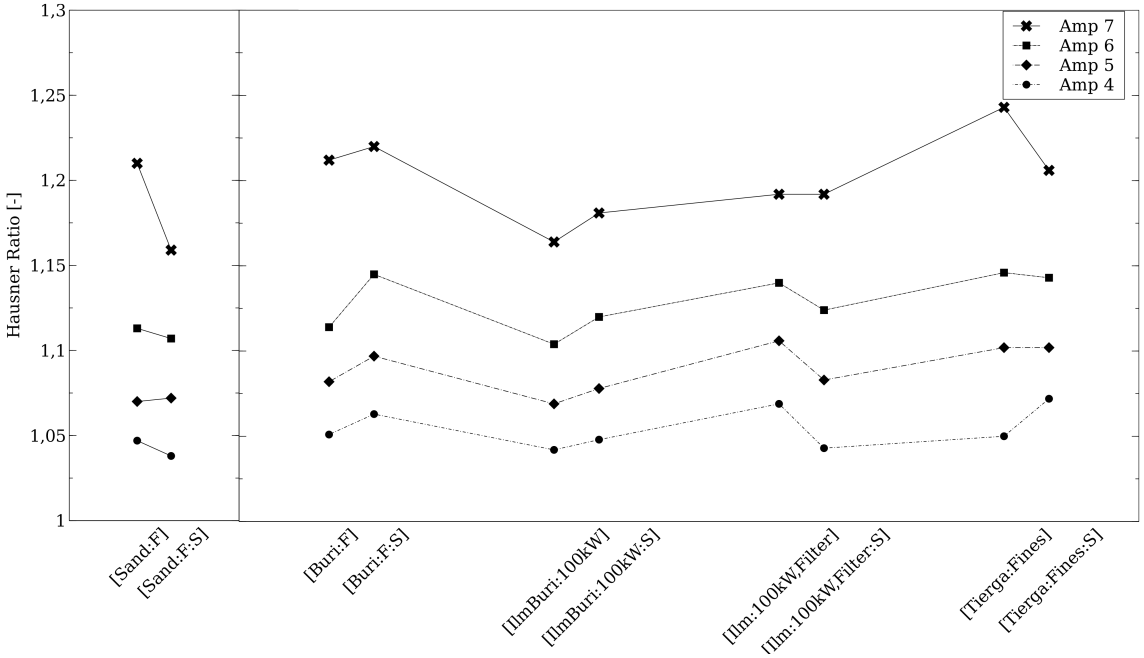

Figure 3.12: Hausner Ratio of remaining carriers

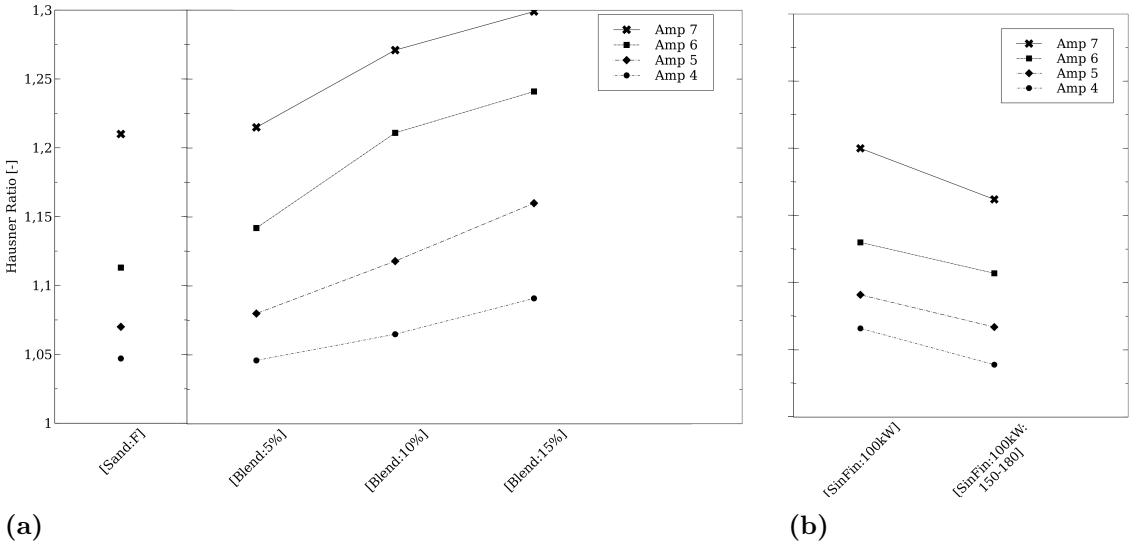

(a) **(b)**

Figure 3.13: Hausner Ratio of blends and of used SinFin

very narrow fraction of 150-180 µm. This comparison is supposed to underline the assumption, that a narrower PSD has a lower HR. In a more uniformly particle environment, particle rearrangement should be less possible. This can be seen, even if the effect is in that case not very large.

3.3.4 Funnel Flow

3.3.4.1 Background

Examining and measuring the flow through a funnel is a very straightforward and simple test. The flow through a hopper can basically occur in two different patterns. These patterns are called mass flow and funnel or core flow. Figure 3.14 illustrates the different regimes. Figure 3.14 a is showing the mass flow, where every particle is in motion as soon as the outlet is opened. This flow pattern is quite steady and controllable. It follows a first in - first out flow sequence.

However funnel flow is characterized by stagnant zones at the wall of the funnel, where particles resist motion. Stagnant zones can vary significantly in size. The most extreme case of funnel flow is the so-called rathole or pipe flow, which is depicted in Figure 3.14 b. [22, 12]

Funnel flow is less predictable and may also lead to undesirable phenomenons like intermittent flow or flooding. These problems are more likely to occur if the material is of cohesive nature. There is the possibility that powder flow stops completely, if a stable arch is formed near the orifice. Particles can interlock and form arches, when adhesive forces are dominant. Especially fine powders have a considerably cohesive strength (also referred as unconfined yield strength or compressive strength) which counteracts the downward weight force. Arches can be metastable in a way that they alternate between an arch condition and a rathole state. This leads to erratic

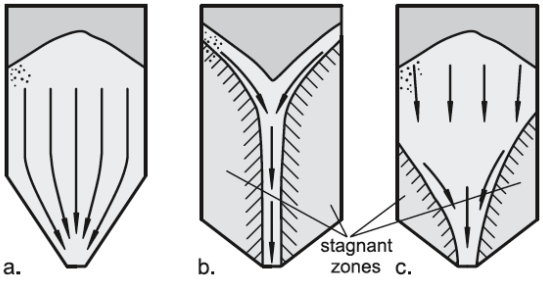

Figure 3.14: Flow pattern during discharge: a. Mass Flow b. Pipe Flow c. Funnel Flow [12]

flow. [22, 12]

Flooding can occur if rathole structures collapse and and air is entrained by falling particles. In this fluidized state powder can flood uncontrollably through the hopper. [22]

3.3.4.2 Setup & Procedure

In order to compare the various carrier materials, the idea was to measure the time, which a defined sample would need to flow through a funnel arrangement. Funnels with different sizes and opening diameters were tested. They all showed the same relation between the materials.

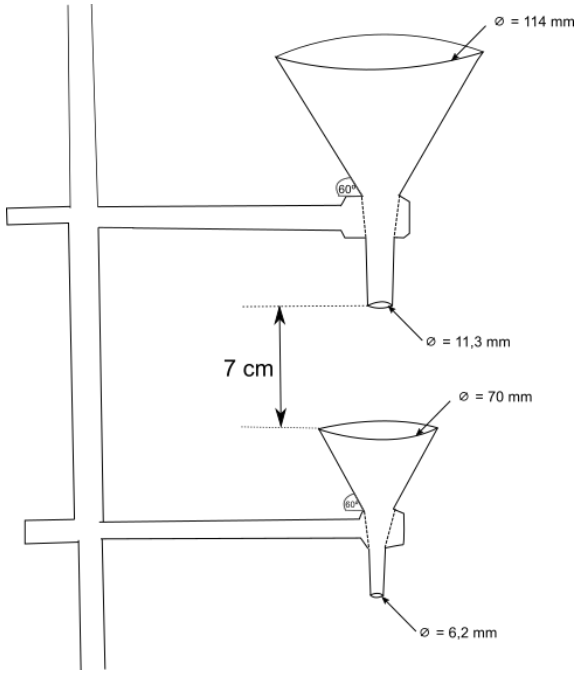

Figure 3.15: Funnel arrangement for flow time measurements

Figure 3.15 shows the funnel setup which was used to measure the flow time. It consists of two different plastic funnels from Pressol Schmiergeräte GmbH with

different outlet diameter. This prolongs the flow time and decreases the chance of errors in terms of clocking. The top funnel was sealed with some device and a sample of 140 g was injected into the funnel. In the moment of removing the seal, flow starts and measuring was conducted accordingly by a stopwatch. This procedure was repeated at least three times. For a better visually experience test were also conducted using a funnel made from transparent plastics, with slightly bigger dimensions than the bottom funnel.

3.3.4.3 Analysis

Besides qualitative observations, such as the flow pattern, the measured flow time was used to investigate differences in the materials. With the flow time and the sample mass, a mass flow was calculated. Furthermore a volume flow based on bulk density was derived. This has the advantage of removing the influence of the densities which obviously play an important role.

3.3.4.4 Results

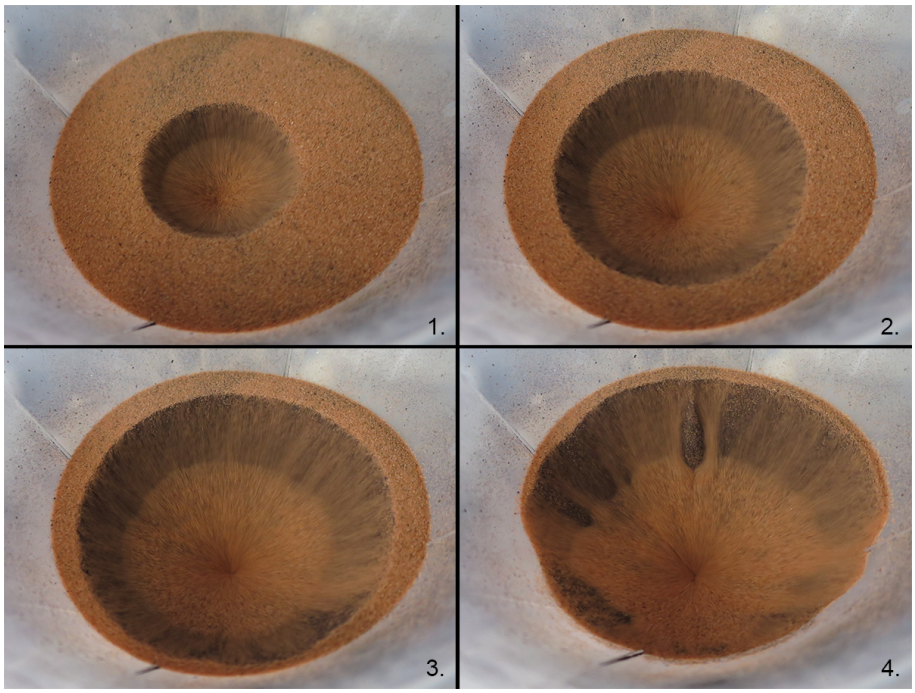

Figure 3.16: Funnel flow pattern

In Figure 3.16 a typical example of the flow pattern is depicted. The material is an artificial blend of 50 % sand and 50 % Tierga Fines (45 µm to 90 µm). It was prepared, as it provides a pattern which can be fairly good investigated and photographed. The flow pattern resembles clearly a core flow. The outer zones remain stagnant until the sinkhole expands and reaches out. This pattern was followed by almost all samples, with the difference that the sinkhole was never that deep and the surrounding material followed much quicker to the center. This

means that this artificial blend has, due to a smaller average grain size, a higher cohesiveness compared to the oxygen carriers.

Problematic flow like erratic flow or ratholing was also only experienced, when investigating artificial blends. In Figure 3.17 a rathole is seen, as it was experienced when

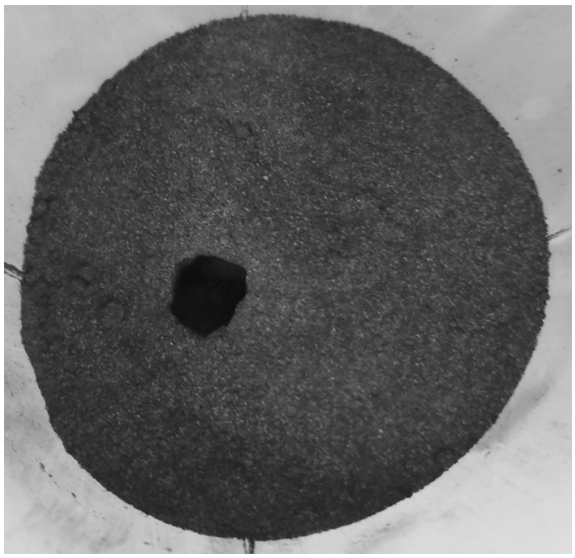

Figure 3.17: A rathole

handling the blends which contained more than 15 % Mangagran Fines [Blend:15%]. Like expected the problems in terms of flowing behavior rose with increased content of fines. With 20 % of Fines ([Blend:20%]) stable arches were formed and free flow was stopped. In addition in several occasions it was possible to observe flooding, which extremely decreased the measured flow time.

Reproducibility in terms of measuring the flow time was good. Given the fact that taking the time was done manually, the deviations were very low.

In figure 3.18 the time measurements of the funnel flow are depicted. Regarding the mass flow differences between the carriers are clearly visible. Since gravity is the driver for flowing and densities differ, those disparities are not surprising. On the other hand the calculated volume flow is much more evenly allocated, almost no differences are visible anymore. One exception is [C14], the used sample flowed comparably bad. Sieving this carrier improved the flow a lot. This stands in contrast to all other carriers, where sieving did not make a big difference.

Regarding the other carriers the picture does not change too much. Not shown here is the comparison of [SinFin:100kW] and the fractionated [SinFin:100kW:150-180], but it showed a minor improvement of the narrow size particles.

More noticeable is the outcome of the blends, which showed severe flooding. Due to this flowing beaviour, much higher values of funnel flow are possible. In the case, where only 5 % fines were added, funnel flow almost tripled in comparison to plain sand. However with increasing content of fines, flow becomes more and more erratic and with 20 % fines there was no flow at all.

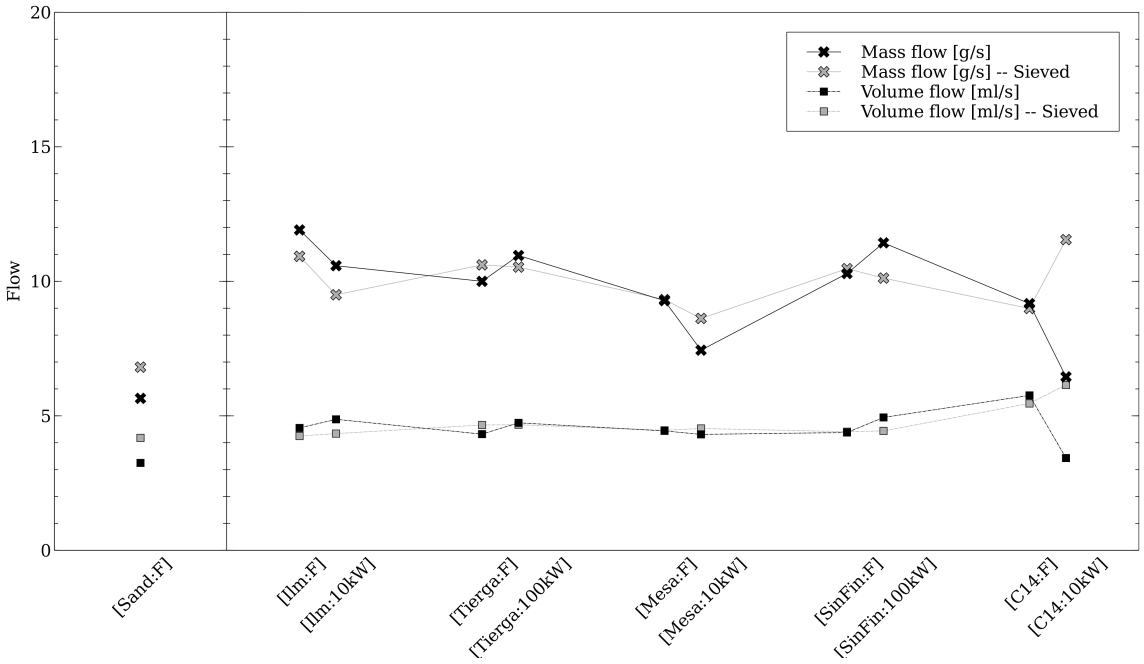

Figure 3.18: Funnel flow time measurements

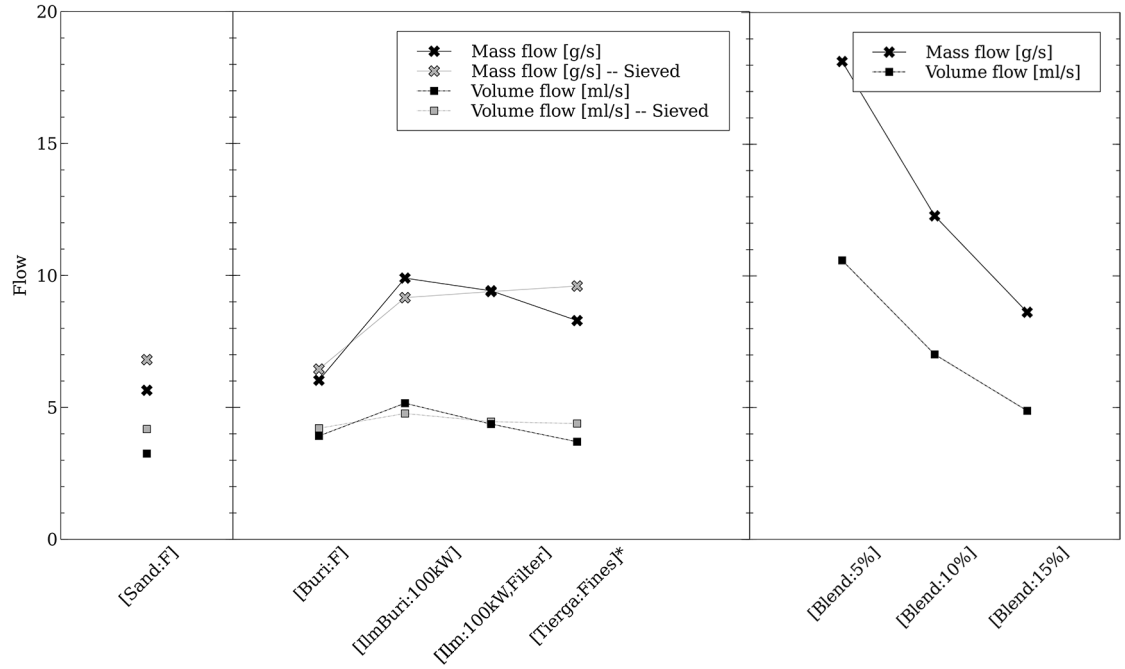

Figure 3.19: Flow time measurements of remaining carriers and blends

3.3.5 Angle of Repose

3.3.5.1 Background

Pouring a powder onto a surface will leave a more or less conical pile of loose, uncompacted bulk solid. The slope of this heap and the horizontal forms an angle, which is defined as the angle of repose. This inclination is considered to be a property of the material. For the formation of the pile, various influences play a role. There are material dependent properties like steric repulsion (geometry), friction and cohesive forces. With an increase of interparticle forces, a steeper slope is expected. The angle of repose is often referred as a static or even intrinsic property of a granular material. But this neglects the effect of the dynamic pouring which is basically the reason for the formation of the heap. The way of conducting the experiment has a huge influence on the final outcome. It makes a difference how the material is poured, from which height and for example which surface material is used. Therefore it is important to keep the setting of the experiment the same and follow a defined procedure. [12, 23]

3.3.5.2 Setup & Procedure

The setup for the test on the angle of repose was quite similar to the two-funnel arrangement described in Chapter 3.3.4.2 and is shown in Figure 3.20. A sample of 140 g is filled in the top funnel. During the filling process the outlet is sealed and removed afterwards to start the flow. A still image of the newly formed heap is taken, using a Canon PowerShot S120. The Camera was mounted on a tripod to ensure reproducible images. The process was repeated thrice.

3.3.5.3 Analysis

The images were post-processed in Adobe Photoshop CS6. The ruler tool was used in order to determine the angle between the horizontal and the slope of the heap. The angles of both sides of the pile were taken into account. An example of such an image is shown in Figure 3.21. The angle in this case for the Tierga ore is 35,4°.

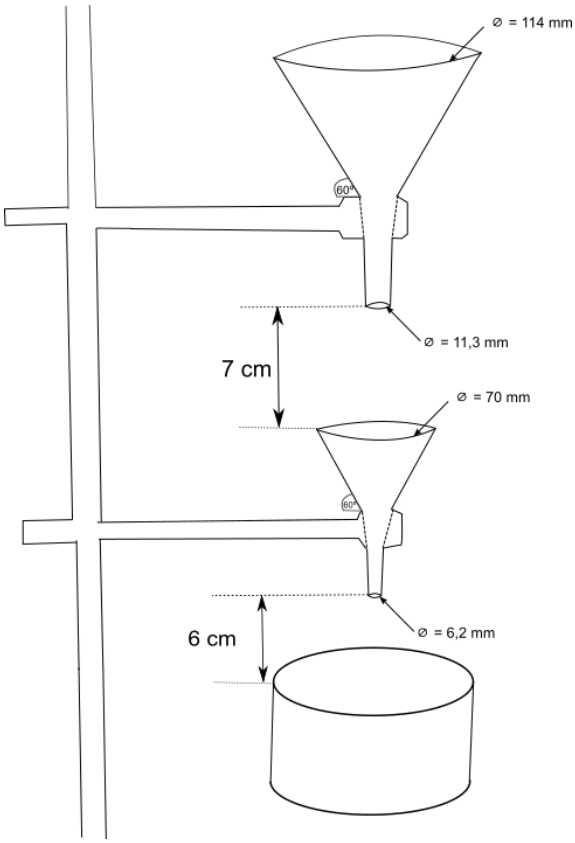

Figure 3.20: Setup for the experimental determination of the Angle of Repose

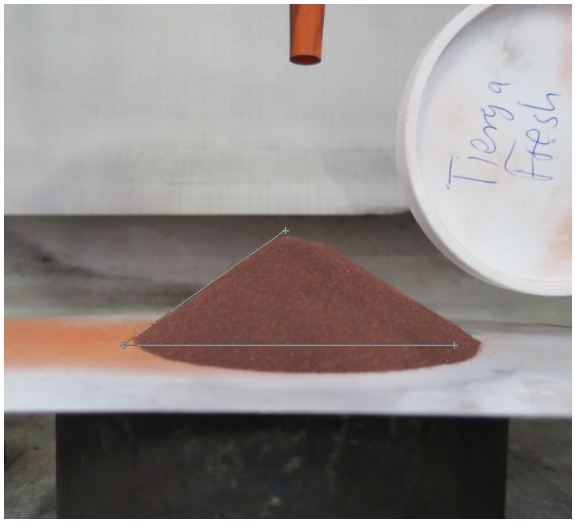

Figure 3.21: Measuring the Angle of Repose

3.3.5.4 Results

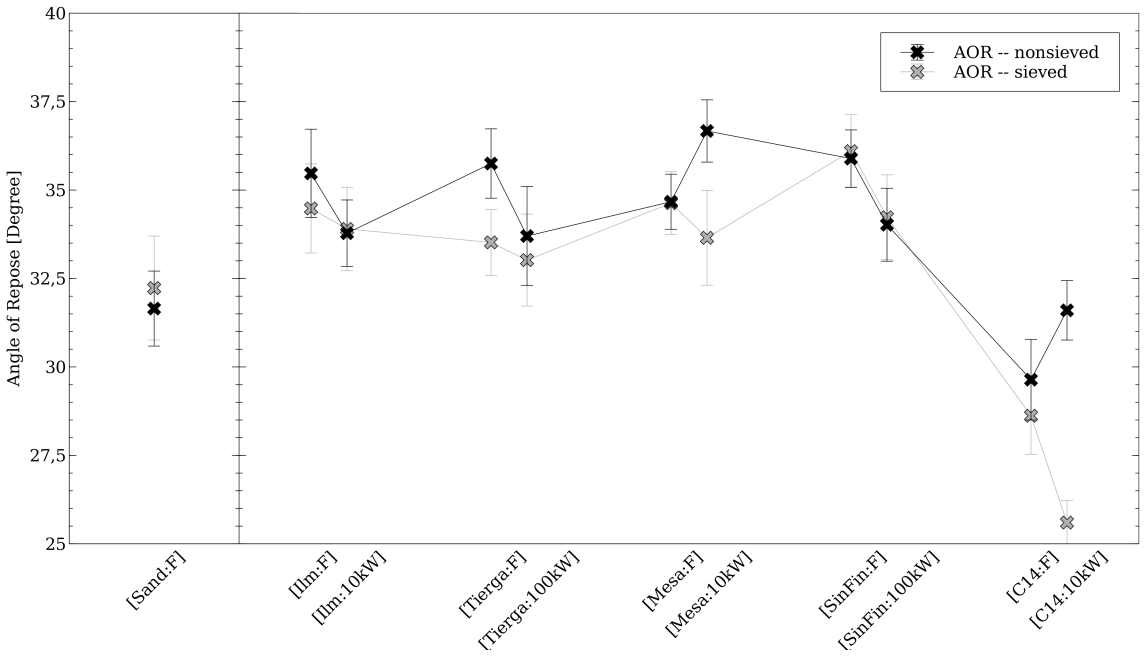

Figure 3.22: Results of the AOR measurements (1)

In figure 3.22 and 3.23 the measured angles of the carriers are plotted. As it could have been expected, the measurements were quite error-prone, since the erection of the heap is a dynamic process. The pile was never perfectly cone-shaped. So the standard deviation of some carriers is up to 1,5 degrees.

Altogether the ores showed slightly higher angles than sand and especially than C14. This synthetic medium can be clearly distinguished, the measured angle is up to 10 degrees below the angle of the ores. Internal friction of C14 is thus comparable low, probably owing to the very spheric particles. Interesting is also the big gap between [C14:10kW] and its sieved counterpart, indicating that in this case the produced fines are responsible for an severe increase of friction. Similar results could be expected for example from [SinFin:100kW], but this is not seen at all. One assumption concerning the angle of repose was, that the angle increases with decreasing grain size, due to increasing interparticular forces. The results from this measurement campaign do not support a strong correlation between the angle of repose and the mean particle size. This can for example be seen in the angle of [Tierga:Fines], which is not larger than the angle of [Tierga:F]. But a correlation can be acknowledged, if the blends are regarded. Here the effect of increasing cohesion is distinct.

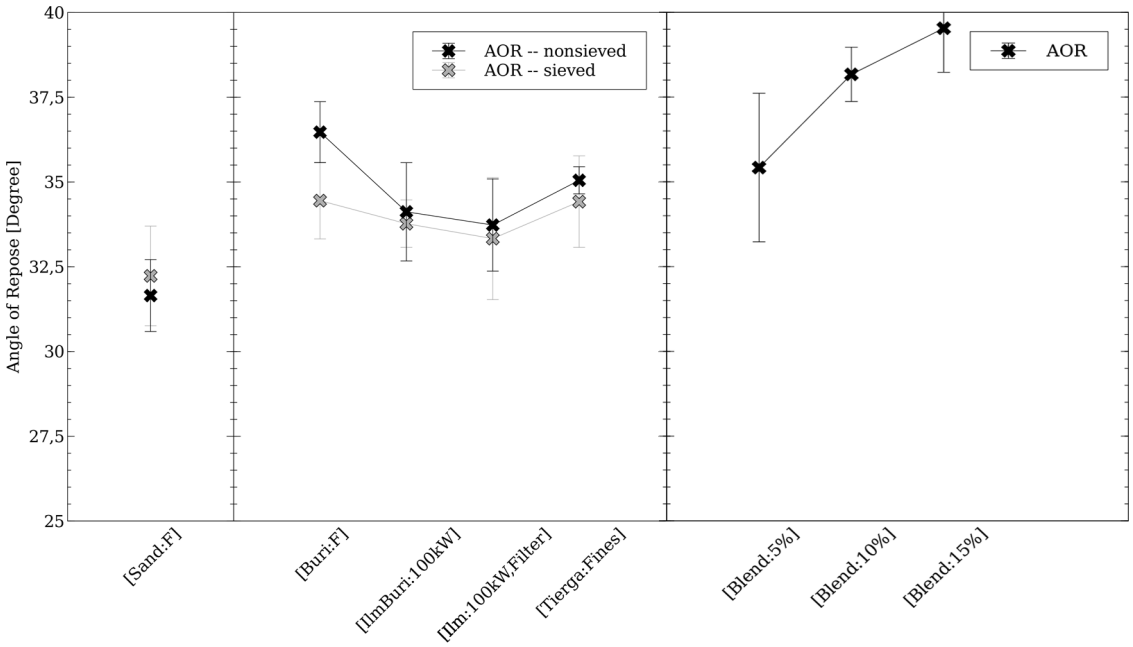

Figure 3.23: Results of the AOR measurements (2)

3.3.6 Minimum Fluidization Velocity

3.3.6.1 Background

The onset of fluidization is well characterized by the the minimum fluidization velocity u_{mf}. Regarding a system, where gas can uniformly flow from bottom to top through a bed of particles, fluidization can be observed as soon as the drag force by the gas becomes greater than the weight of particles. Thus the minimum fluidization velocity is defined when those forces are in equilibrium. From measuring the pressure drop over the bed, while increasing and decreasing the volume flow of gas, a Δp-versus-u_o diagram can be plotted. u_o is the superficial velocity and can be derived from volume flow. This graph is particularly useful in order to investigate the minimum fluidization velocity. It is depicted in Figure 3.24 for uniformly sized sand as bed material. Initially the pressure drop increases proportional to gas velocity

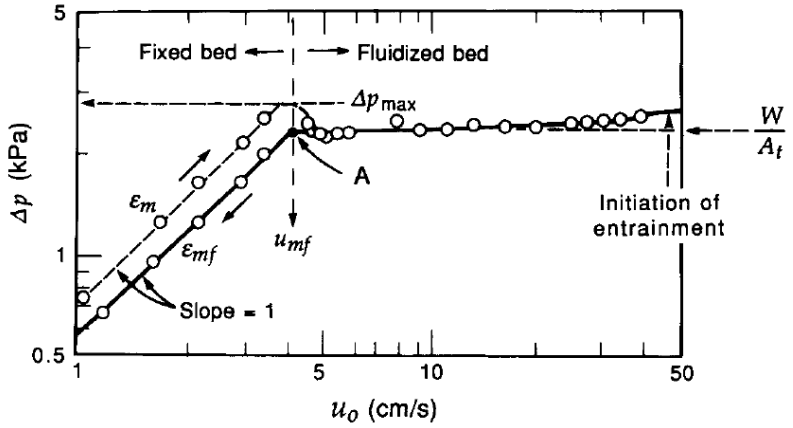

Figure 3.24: Δp-versus-u_o for uniformly sized sharp sand [24]

because energy is „lost“ due to friction between gas and solids. It can be assessed by Ergun's equation of frictional pressure drop, in which pressure drop is correlated to both viscous and inertia related effects.

At some point the pressure drop will not increase anymore but will stay fairly constant. Meaning that the bed „unlocks“and expands, the voids between the particles grow larger. So the drag also remains constant until particles are getting entrained and carried away. As seen in the graph the transition is marked by the u_{mf}. The hysteresis between aeration and deaeration is a result of consolidation in the fixed bed.

u_{mf} can be estimated by using the equilibrium of geodetic pressure drop and empirical pressure drop (e.g. Ergun). An equation for the calculation can be found in Kunii and Levenspiel's Fluidization Engineering, Chapter 3, Eq. 18. [24] This equation shall be used to compare experimental and estimated values.

Fluidization can occur in different regimes like bubbling, slugging or channeling. Which regime actually takes place, is dependent on gas properties and probably more important on the properties of the bed material. Geldart proposed a classification for particles, which assigns fluidization behavior to particle properties. The important

properties therefore are particle density and particle size. The classification is shown in Figure 3.25.

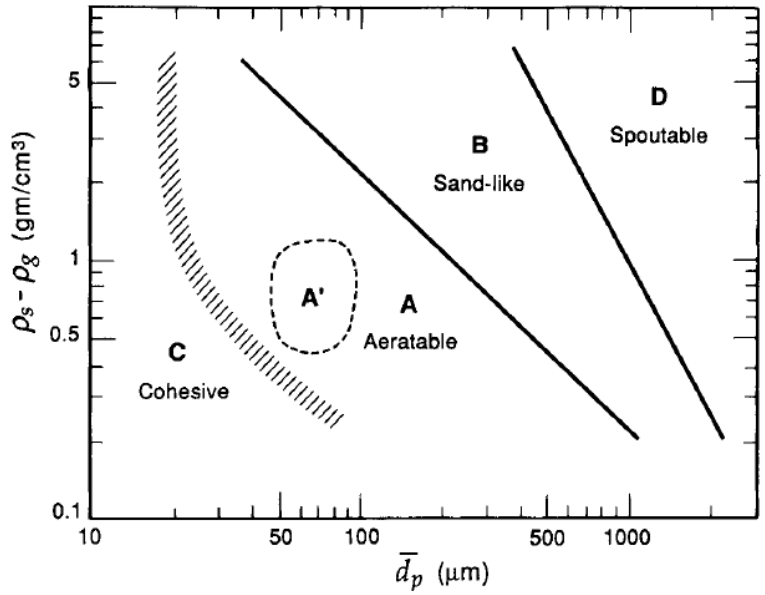

Figure 3.25: Geldart classification of particles for air at ambient conditions [24]

3.3.6.2 Setup & Procedure

The fluidization of carrier particles was conducted in a tube made from acrylic glass. The tube's length was 1 m and it's inner diameter 74 mm. It was mounted on top of a wind box, which contained the pressure tap and the air supply. Between the wind box and the tube, a perforated metal plate and a cellulose filter took care of proper gas distribution. This assembly also prevented particles from entering the wind box. A high pressure drop over the gas distributor ensures equal flow over the entire cross section of the bed. To address this requirement, a cellulose filter was found which provided a sufficient pressure drop in all conditions. The pressure drop of the distributor is supposed to be at least 20 % of the pressure drop across the bed. [25]

The pressure tap from the wind box was connected to a pressure transducer (Honeywell 163PC01D36). For the second connection of the transducer ambience was used, as the tube opened on top to the ambient air. Variation of the mass flow of the air was achieved by two mass flow controllers. Mass flow controller and pressure transducer were connected to a labview environment, which controlled and recorded the process.

A sample of around 300 g was weighed and inserted into the tube. To get rid of possible consolidation effects, the material was initially fluidized for some time. Bed height was read, using a ruler. To obtain data for drawing Δp-versus-u_o diagrams, volume flow was then incrementally increased until thorough fluidization was visible. Afterwards volume flow was reduced, following the same steps. The step range was

one or two liters per second, each step was kept until pressure measurements were within the same range for some time.

3.3.6.3 Analysis

Raw data from measurements contained volume flow versus total pressure drop. Required parameters for determining u_{mf} are superficial velocity versus pressure drop across the bed. The superficial velocity can be calculated from volume flow and cross area of the tube by Equation 3.15.

$$u_o = \frac{\dot{V}}{A_i} = \frac{\dot{V}}{\frac{1}{4}\pi d_i^2} \tag{3.15}$$

To acquire the pressure drop across the bed, the pressure drop from the plate and the filter had to be considered. The pressure drop of solely the distributor was measured and a linear regression was found to fit this pressure drop. This correlation was then used to get the actual pressure drop from the bed.

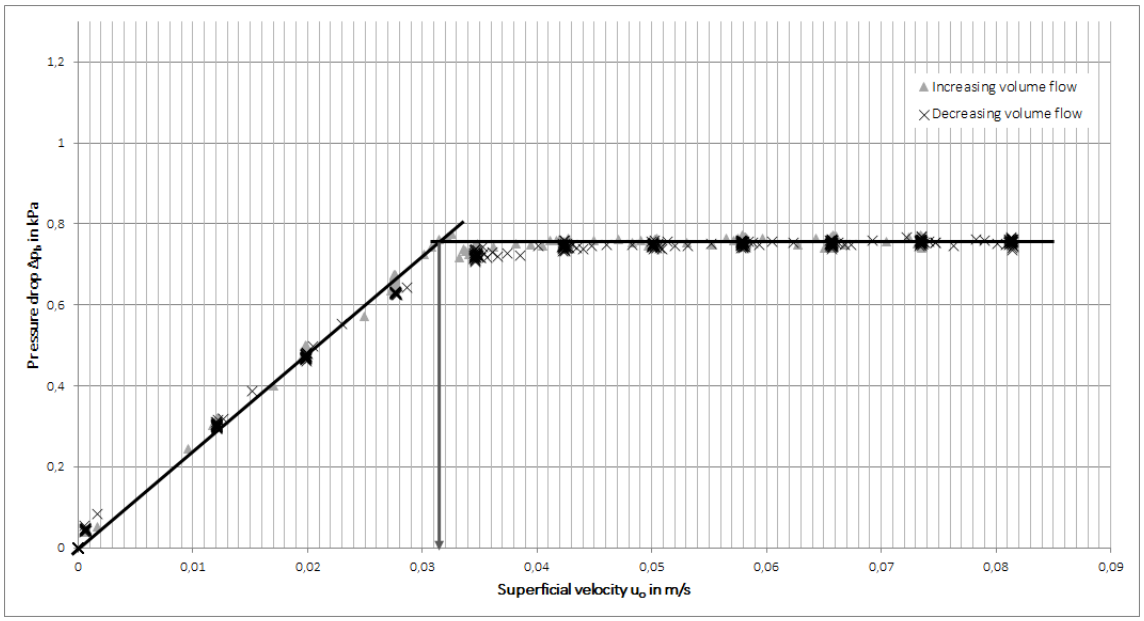

Figure 3.26: Δp-versus-u_o for used Ilmenite

Figure 3.26 shows Δp-versus-u_o of used Ilmenite, which was experimentally established. It resembles the plot from literature (Figure 3.24) quite well, the exaltation owed to consolidation is also visible.

All investigated materials have a relatively broad particle size distribution and thus there is no sharp transition between fixed and fluidized bed. In this case it is common to draw two lines, one with the slope of frictional pressure drop and the other depicts the stagnant fluidized state. The intersection determines the value for the minimum fluidization velocity. In the case of used Ilmenite it is around 0,031 m/s.

For the analytical estimation several assumptions have to be made. Particle size, sphericity and true particle density are the most important influencing parameters

on particle side. None of those is readily known. For the particle size it is most straightforward to use the mean value, derived from sieving. Sphericity was assumed to be equal to the compactness, which was established from microscopy, even though the values are probably not perfectly suited to resemble sphericity. While sphericity is volume based, compactness refers to area. So from a more consistent point of view, 2d values could be correlated to volume. True particle density measurements are not available, instead the measured tapped density served as basis for estimation. By assuming the voidage in this dense packing, estimation can be done easily. Correlations between sphericity and voidage for different packed beds can be found in Kunii and Levenspiel. [24] The correlation is strictly speaking only valid for uniformly sized particles, but nevertheless it was used here to assess void fractions.

3.3.6.4 Results

Fluidization of the different materials was easily possible. All showed relatively similar behavior. With reaching the minimum fluidization velocity instant bubbling occurred. Bubbles rose fast and grew larger with increasing superficial velocity. Radical shut down of gas supply leaded to immediate collapse of the bed. These are characteristics of particles, which can be classified in Geldart group B.

Part of the data evaluation was to make sure, that there is a sufficient pressure drop over the distributer plate compared to the pressure drop over the bed. Due to the broad range of materials and respectively the broad range of fluidization velocities, the pressure drop of the distributer varied significantly. However it never fell below 20 % or exceeded 250 %. Most of the time pressure drop was around 40 - 50 %, which is considered an ideal value.

The fact, that some carriers posses a broad PSD was not only visible in the Δp-versus-u_o plots, but could also be seen in preliminary partial fluidization of small particles at the surface. Table 3.4 and 3.5 lists the important particle properties, which have been estimated according Chapter 3.3.6.3. With these properties u_{mf} values were calculated and compared to the experimentally measured values. Note: the voidage ϵ_m given here is for a densely packed bed, as you would expect from tapping. For the final calculation of u_{mf} slightly higher values were used.

Table 3.4: u_{mf}: particle properties and results for fresh material

		[Sand:F]	[Ilm:F]	[Tierga:F]	[Buri:F]	[C14:F]	[Mesa:F]	[SinFin:F]
Sphericity Ψ_s	[-]	0,88	0,80	0,92	0,83	1,00	0,72	0,82
Voidage ϵ_m	[-]	0,38	0,40	0,37	0,39	0,36	0,44	0,39
Particle density	[kg/m^3]	2805	4361	3673	2522	2486	3731	3854
$x_{50,3}$	[µm]	132,4	218,4	160,3	158,8	151,4	238,6	195,4
u_{mf} calculated	[m/s]	0,016	0,076	0,029	0,023	0,016	0,087	0,052
u_{mf} measured	[m/s]	0,015	0,071	0,035	0,031	0,03	0,074	0,049

The comparison is depicted in figure 3.27 and figure 3.28. Considering the assumptions made for the calculations, the accordance is not too bad. In the right graph

Table 3.5: u_{mf}: particle properties and results for used material

		[Ilm: 10kW]	[Tierga: 100kW]	[IlmBuri: 100kW]	[C14: 10kW]	[Mesa: 100kW]	[SinFin: 100kW]	[Ilm: Filter]	[Tierga Fines]
Sphericity Ψ_s	[-]	0,81	0,90	0,83	1,00	0,62	0,83	0,80	0,90
Voidage ϵ_m	[-]	0,40	0,37	0,39	0,36	0,46	0,39	0,40	0,37
Particle density	[kg/m^3]	3618	3673	3144	2936	3201	3794	3590	3556
$x_{50,3}$	[µm]	180,5	181,1	190,2	125,2	273,2	162,4	152,3	96
u_{mf} calculated	[m/s]	0,043	0,038	0,04	0,013	0,113	0,035	0,031	0,011
u_{mf} measured	[m/s]	0,031	0,04	0,04	0,014	0,105	0,03	0,029	0,016

in figure 3.28 the influence of particle size distribution is investigated. The difference between regular used Sinfin and narrow sized used Sinfin is small. The sieving process led to a slightly higher mean particle size, which would support a slightly higher u_{mf}. Thus it is questionable, if a broader PSD has an effect on u_{mf} at all.

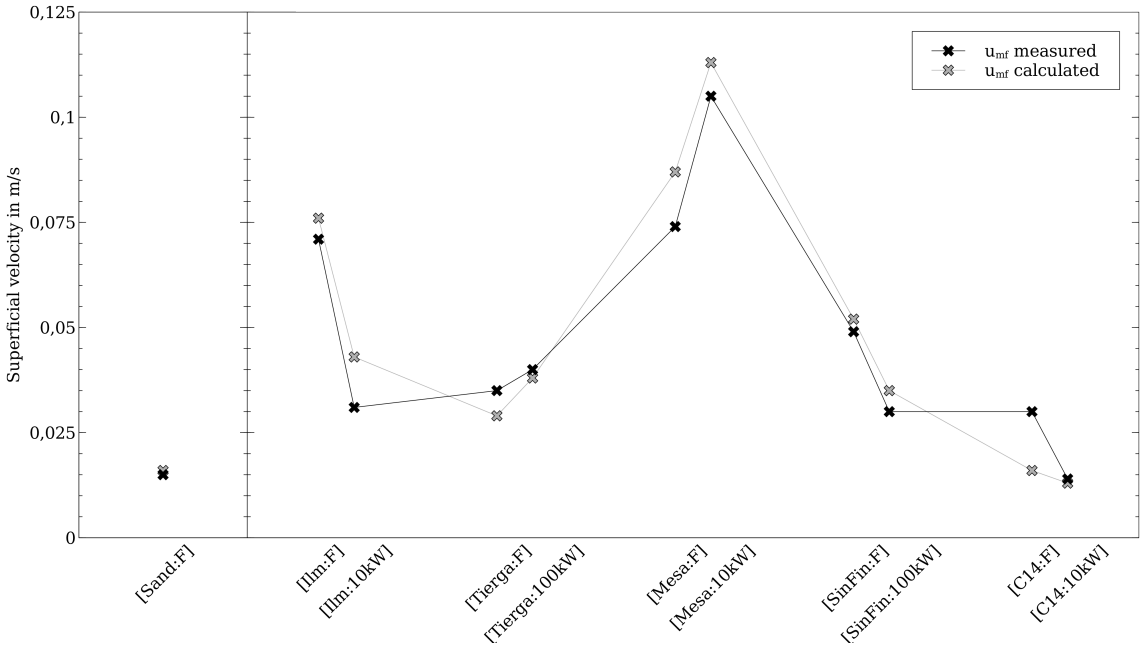

Figure 3.27: Experimental vs calculated u_{mf} values (1)

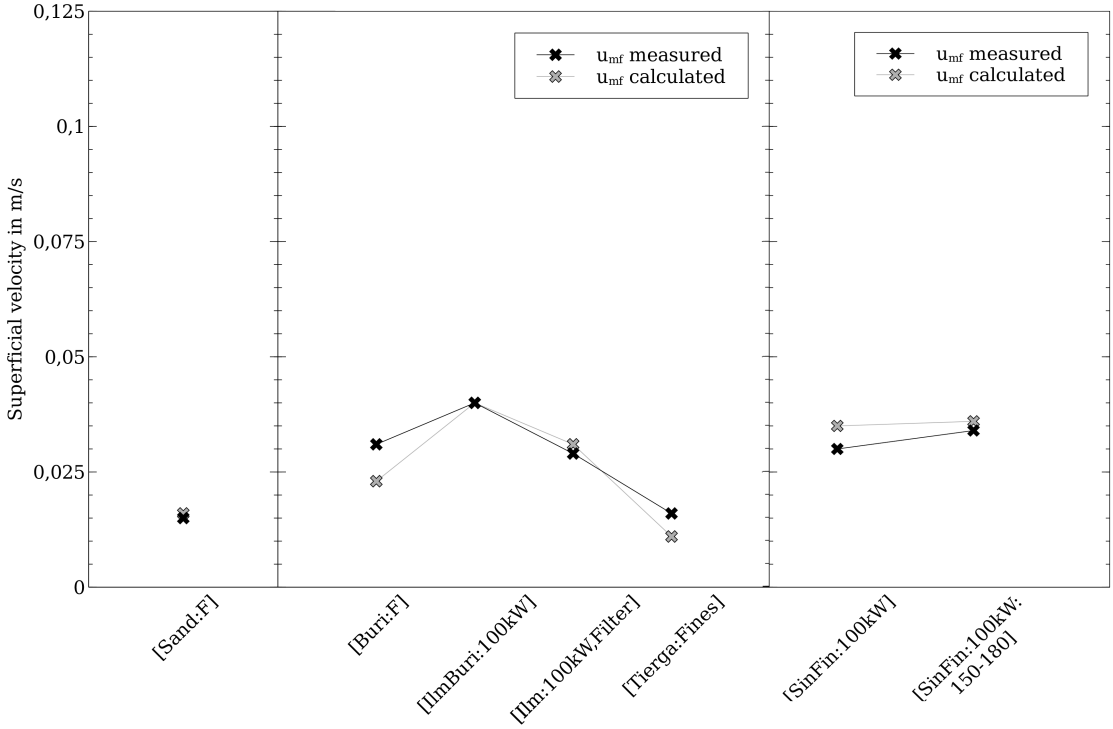

Figure 3.28: Experimental vs calculated u_{mf} values (2)

4

Overall results

The aim of the work was to evaluate the flowability in a comprehensive way and state which carrier flows well and which does not. This should ultimately create a scientific knowledge enabling the prediction of the behavior of a given material, based on few experiments.

Previous considerations and experiments addressed a variety of relevant parameters, but until now they were not linked. There is no characteristic value for flowability which can be simply computed. However in this work there is an attempt to make a simple statement based on the results gained from experiments. In order to compare outcomes from the different experiments, standardization is required. This can be done using a statistical method, known as standard score or z-score. It transforms a random variable in a way that the new variable has an expected value of zero and variance of one. Transformation is performed by applying equation 4.1 for each variable.

$$z = \frac{x - \mu}{\sigma} \tag{4.1}$$

z is the transformed new variable, while x represents the original variable. μ and σ are the mean and the standard deviation of the probability distribution, i.e. the distribution of experimental results. [26] For each material and each experiment standard scores were calculated and ultimately added up to a final score. By assigning plus or minus signs to the partial scores, the added up score will indicate the flowability. A plus sign signifies better flowability, a minus worse. Furthermore the uncertainties from the experiments were taken into account.

The scored experiments are shortly recapitulated from previous chapters:

- AOR - higher degree implies higher internal friction, indicating worse flowability
- Funnel flow - higher volumetric flow indicates better flowability
- HR - higher values indicates more cohesiveness and thus worse flowability

Another possibility would be to include the minimum fluidization velocity in the score. This alternative score is presented in Appendix C.

Table 4.1 lists the experimental outcomes for the fresh materials. With the Mean and the standard deviation, depicted in table 4.2, the scores can be computed. Partial scores and overall score is shown in table 4.3.

Table 4.1: Values for derivation of the flowability score

		[Sand:F]	[Ilm:F]	[Tierga:F]	[C14:F]	[Mesa:F]	[SinFin:F]
AOR	[°]	31,65	35,47	35,75	29,64	34,67	35,89
Funnel flow	[ml/s]	3,25	4,55	4,32	5,76	4,44	4,38
HR	[-]	1,210	1,190	1,239	1,129	1,187	1,181

Table 4.2: Mean and standard deviation

		Mean μ	σ
AOR	[°]	34,18	2,72
Funnel flow	[ml/s]	4,67	1,45
HR	[-]	1,2	0,04

Table 4.3: Scores

		[Sand:F]	[Ilm:F]	[Tierga:F]	[C14:F]	[Mesa:F]	[SinFin:F]
AOR	[°]	0,93	-0,47	-0,58	1,67	-0,18	-0,63
Funnel flow	[ml/s]	-0,98	-0,08	-0,24	0,75	-0,16	-0,2
HR	[-]	-0,24	0,25	-0,95	-0,3	1,76	0,48
Score (AOR, Flow, HR)		-0,29	-0,3	-1,77	4,19	-0,01	-0,35

The sign of values is already altered in a way that a positive sign signifies better flowability and a negative sign signifies worse flowability. According to this method concerning the fresh material C14 is the best ”flowing” material, because it has the highest positive score. On the other hand Tierga is considered worst.

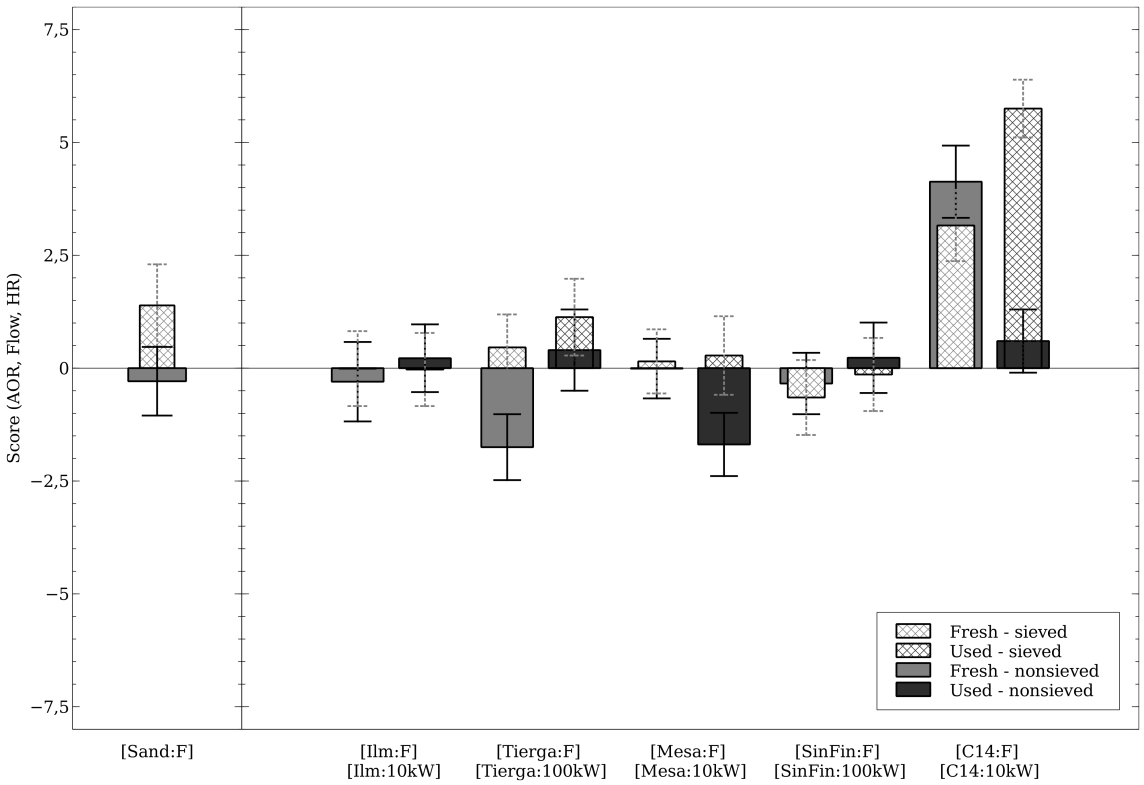

Figure 4.1: Flowability score (AOR, Flow, HR)

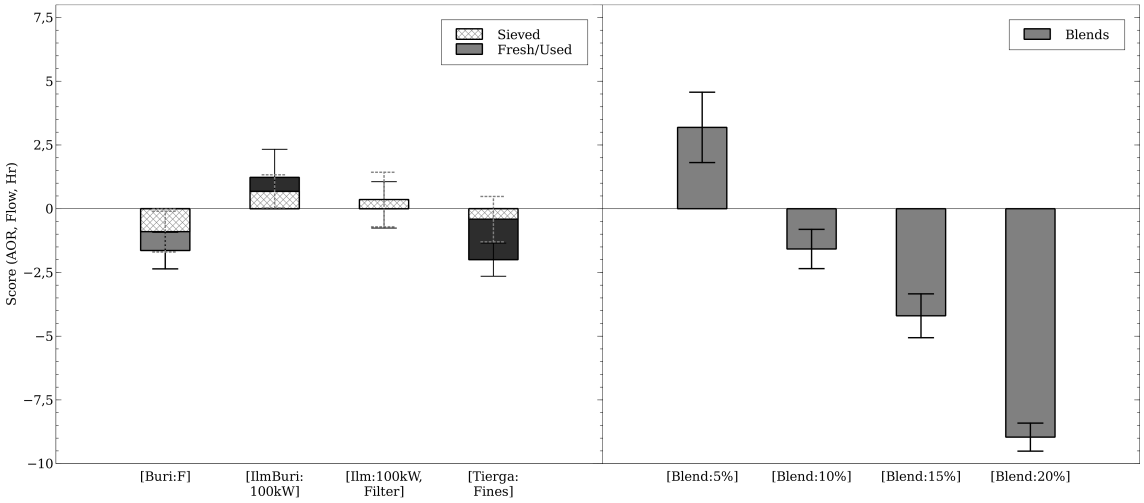

Figure 4.2: Flowability score (AOR, Flow, HR)

Figure 4.1 and 4.2 depicts the results for the comparison on flowability. Detailed values are found in Appendix B, table B.1 - B.8.

Neglecting the blends, [Tierga:F], [Mesa:10kW], [Buri:F] and [Tierga:Fines] are the materials which scored worst. Their score is around -2. On the other hand is [C14:F] outstanding, scoring way better than any other non-sieved carrier. Regarding the flowability trend from fresh to used condition, there might be a slight improvement for Ilmenite, Buritirama and SinFin, while Mesa and C14 distinctly decrease their flowability. Again Tierga is not suited for direct comparison, due to addition of larger particles during operation.

Sieving would be readily expected to increase flowability. The scores indicate, that this is not essentially the case for all investigated materials. But it is very clearly true for [C14:10kW], which score increased almost tenfold.

The blends show an interesting result, the score of [Blend:5%] is positive and exceeds plain [Sand:F] significantly. With increasing content of fines, flowability gets rapidly worse: 20% of fines leading already to a score of around -9. While the decrease of flowability is expected, the initial positive value of [Blend:5%] needs an explanation. With the help of the partial scores, it can be derived that the funnel flow contributes largely to the positive value, while AOR and HR are negative. The blends developed a flow pattern in the funnel, which was somewhat different to the other materials. It is called flooding. Flooding decreases the flow time significantly, but it is also rather unpredictable and uncontrollable.

Adding the different experiments to a flowability score, raised the question how the experiments are linked and if there is some kind of correlation. Figure 4.3 correlates the different experimental outcomes in four different ways. At first glance the points seem quite scattered, but even though correlations might be recognizable. The first graph shows AOR vs. u_{mf}. With increasing angle the minimum fluidization tends also to increase. This would make sense, as a higher cohesive character should prevent fluidization. Regarding the blends, there is no correlation between u_{mf} with AOR. This not surprising, as the fines from the blends are elutriated almost instantly during the u_{mf} measurements. This unmixing effect is clearly reflected in the graph.

The graph top right displays HR vs. Mean particle diameter. A high HR would be expected to correlate with a small mean particle size. This trend is not distinctly visible for the investigated particle size range. It seems rather stagnant or only slightly correlating. For the blends of course the trend is clear.

The figure depicting AOR vs. HR supports previous considerations that larger adhesive forces can be seen as well from a higher AOR and from a higher HR. The correlation is particularly well established for the blends.

In the last figure volume flow is plotted against Hausner Ratio. If the Hausner Ratio of a material is higher, it seems to flow worse through the funnel. This is the behavior which would have been expected. The trend concerning the blends follows the same pattern, but because of the flooding on another baseline and with a much steeper slope.

The trends from the graphs are not ultimately distinct, but this is not really sur-

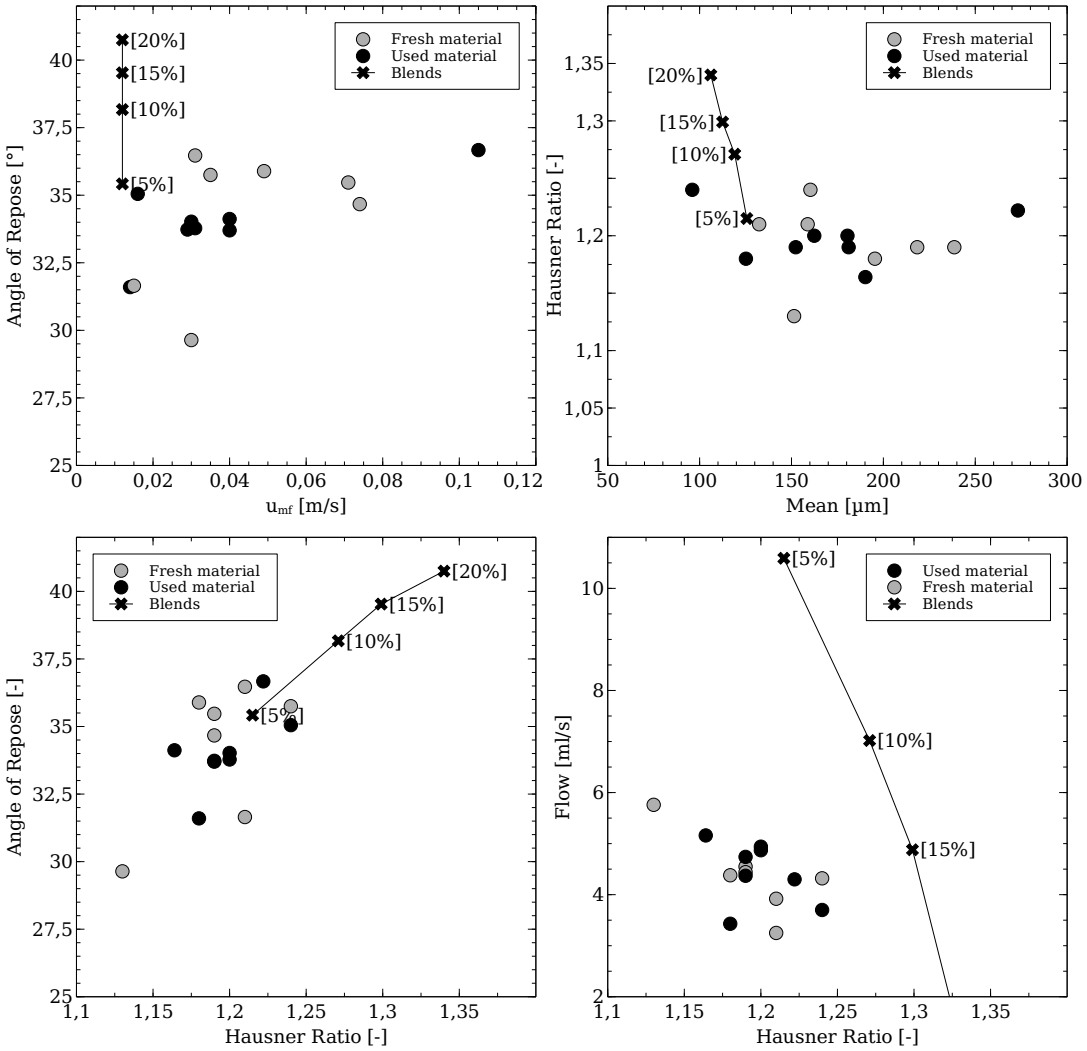

Figure 4.3: Correlation analysis

prising, as the investigated materials also differ in many ways. To establish comprehensive correlations another stock of material should have been used.

5

Conclusion

Starting from peculiar observations in the CLC operation, the flowability of oxygen carriers was determined as matter of a thorough investigation. The carriers involved in this work were iron ores, manganese ores and a synthetic material. If available, samples were taken from fresh and used condition. Additionally blends were prepared which contained sand and very fine particles. They could deliver meaningful information about the influence of fines on flowability.

The investigation included a theoretical part in which the relevance of particle forces was pointed out. Van der Waals forces for dry particles and liquid bridges for moist particles are determining the cohesive nature of the collective. They rely strongly on contact areas i.e. distance between particles and thus particle size and shape play an important role regarding adhesive forces.

To access the particle size distribution sieving was conducted. The Mean and the standard deviation of the distribution were chosen to describe the PSD. Most particles ranged between 150 µm and 200 µm. The shape of the particles was approached by digital imaging using a light microscope. A 2d value was established in order to compare the shape of the different carriers. Compactness values were mostly around 0,8 to 0,9.

With the aim of gathering more information about the apparent adhesive forces under different circumstances, four different experiments were introduced. The flow through a funnel, the angle of repose and the Hausner ratio are comparative methods to observe flowing behavior in static as well as in dynamic situations. Determining minimum fluidization velocities was seen as a way to acknowledge the fact fluidization plays an important role in CLC.

Generally all investigated material, except the blends, behaved quite well in terms of flowing. There was no sign of strange flow pattern like erratic flow. However some differences were seen and confirmed by the measurements.

Those differences are reflected in the flowability score, which was developed in order to simplify the experimental outcome.

The score was established by means of statistical standardization. The experiments involved are based on well-known bulk investigations and address the nature of adhesive forces in different ways.

The importance of including various properties and results was proved. A material might flow very well through the funnel, but at the same time it can hold a high

angle of repose, which is considered bad in terms of flowability.

The score is based on a rather small population and attention should be paid on the limits of such a score. It was tailored for a specific set of oxygen carriers, which are essentially free flowing and results may not be transferable to another stock of materials.

The overall results from the work indicate that flowability of oxygen carriers is not a major concern for the CLC operation. But since the experiments were carried out at ambient conditions, a high temperature effect on flowability can not be inherently ruled out.

Regarding the individual carriers, it is possible to draw some conclusions.

- Synthesized materials as [C14:F] seem superior in terms of flowability, but serious attrition during operation can diminish this ability.
- Ores as seen in [Ilm], [SinFin] and [IlmBuri] seem to increase their flowability due to operation.
- Most of the carriers are scoring in the same range as sand (-2 to 2). Compared to the blends ($\sim$ -9), this indicates good overall flowability.

Future work could be done by investigating more materials, weighting the results in another way or by further improving the existing experimental methods. Moreover it would be interesting to address the topic of fines in a more detailed way. The effect of very fine material is somewhat indistinct, they may act assisting or not (see chapter 2.3). Nowadays fines are regarded as particles with a grain size below 45 µm. This is rather unspecific, so the first thing that could be done in this respect is assessing the real size range of what is now called fines.

References

[1] Dr. Peter Tans and Dr. Ralph Keeling. *Trends in Atmospheric Carbon Dioxide*. U.S. Department of Commerce, National Oceanic & Atmospheric Administration. Sept. 16, 2015. URL: www.esrl.noaa.gov/gmd/ccgg/trends.

[2] D. Lüthi et al. *800.000-year Ice-Core Records of Atmospheric Carbon Dioxide*. NOAA/NCDC Paleoclimatology Program. 2008. URL: http://cdiac.ornl.gov/trends/co2/ice_core_co2.html.

[3] B. Metz and Intergovernmental Panel on Climate Change. Working Group III. *Carbon Dioxide Capture and Storage: Special Report of the Intergovernmental Panel on Climate Change*. 25 CM. Cambridge University Press, 2005. ISBN: 9780521866439.

[4] Carl Linderholm. *CO_2 capture using Chemical-Looping Combustion : Operational Experience with Gaseous and Solid Fuels*. Gothenburg, Sweden: Chalmers University of Technology, 2011. ISBN: 9789173855181.

[5] Anders Lyngfelt, Bo Leckner, and Tobias Mattisson. "A fluidized-bed combustion process with inherent CO_2 separation; application of chemical-looping combustion". In: *Chemical Engineering Science* 56.10 (2001), pp. 3101–3113. ISSN: 0009-2509. DOI: http://dx.doi.org/10.1016/S0009-2509(01)00007-0.

[6] Anders Lyngfelt and Bo Leckner. "A 1000 MW_{th} boiler for chemical-looping combustion of solid fuels - Discussion of design and costs". In: *Applied Energy* (2015). ISSN: 0306-2619. DOI: http://dx.doi.org/10.1016/j.apenergy.2015.04.057.

[7] Pontus Markström, Carl Linderholm, and Anders Lyngfelt. "Chemical-looping combustion of solid fuels - Design and operation of a 100 kW unit with bituminous coal". In: *International Journal of Greenhouse Gas Control* 15 (2013), pp. 150–162. ISSN: 1750-5836. DOI: http://dx.doi.org/10.1016/j.ijggc.2013.01.048.

[8] Carl Linderholm et al. "Material balances of carbon, sulfur, nitrogen and ilmenite in a 100 kW CLC reactor system". In: *International Journal of Greenhouse Gas Control* 27 (2014), pp. 188–202. ISSN: 1750-5836. DOI: http://dx.doi.org/10.1016/j.ijggc.2014.05.001.

[9] Jochen Ströhle, Matthias Orth, and Bernd Epple. "Chemical looping combustion of hard coal in a 1 MW_{th} pilot plant using ilmenite as oxygen carrier". In: *Applied Energy* (2015). ISSN: 0306-2619. DOI: http://dx.doi.org/10.1016/j.apenergy.2015.06.035.

[10] Magnus Rydén et al. "Combined oxides as oxygen-carrier material for chemical-looping with oxygen uncoupling". In: *Applied Energy* 113 (2014), pp. 1924–1932. ISSN: 0306-2619. DOI: http://dx.doi.org/10.1016/j.apenergy.2013.06.016.

[11] Mohammad M. Hossain and Hugo I. de Lasa. "Chemical-looping combustion (CLC) for inherent separations - a review". In: *Chemical Engineering Science* 63.18 (2008), pp. 4433–4451. ISSN: 0009-2509. DOI: http://dx.doi.org/10.1016/j.ces.2008.05.028.

[12] D. Schulze. *Powders and Bulk Solids: Behavior, Characterization, Storage and Flow*. Springer Berlin Heidelberg, 2007. ISBN: 9783540737681.

[13] J.P.K. Seville, C.D. Willett, and P.C. Knight. "Interparticle forces in fluidisation: a review". In: *Powder Technology* 113.3 (2000). Neptis Symposium on Fluidization - Present and Future, pp. 261–268. ISSN: 0032-5910. DOI: http://dx.doi.org/10.1016/S0032-5910(00)00309-0.

[14] Niklas Sandler et al. "Effect of Moisture on Powder Flow Properties of Theophylline". In: *Pharmaceutics* 2.3 (2010), p. 275. ISSN: 1999-4923. DOI: 10.3390/pharmaceutics2030275.

[15] Igino Tomasetta. "The effect of temperature on flow properties of powders". PhD thesis. 2012.

[16] M. Stieß. *Mechanische Verfahrenstechnik*. Springer-Lehrbuch Bd. 2. Springer Berlin Heidelberg, 2013. ISBN: 9783662085998.

[17] T. Allen. *Particle size measurement*. Powder Technology Series. Springer US, 2013. ISBN: 9781489930637.

[18] Bhesh Bhandari. *Handbook of Food Powders, Processes and Properties*. Cambridge, UK: Woodhead Publishing, 2013. ISBN: 978-0-85709-513-8.

[19] M. Stieß. *Mechanische Verfahrenstechnik - Partikeltechnologie 1*. Springer-Lehrbuch. Springer Berlin Heidelberg, 2008. ISBN: 9783540325529.

[20] E.C. Abdullah and D. Geldart. "The use of bulk density measurements as flowability indicators". In: *Powder Technology* 102.2 (1999), pp. 151–165. ISSN: 0032-5910. DOI: http://dx.doi.org/10.1016/S0032-5910(98)00208-3.

[21] K. Traina et al. "Flow abilities of powders and granular materials evidenced from dynamical tap density measurement". In: *Powder Technology* 235 (2013), pp. 842–852. ISSN: 0032-5910. DOI: http://dx.doi.org/10.1016/j.powtec.2012.11.039.

[22] James K Prescott and Roger A Barnum. "On powder flowability". In: *Pharmaceutical technology* 24.10 (2000), pp. 60–85.

[23] G. Lumay et al. “Measuring the flowing properties of powders and grains”. In: *Powder Technology* 224 (2012), pp. 19–27. ISSN: 0032-5910. DOI: http://dx.doi.org/10.1016/j.powtec.2012.02.015.

[24] Daizo Kunii and Octave Levenspiel. “Chapter 3 - Fluidization and Mapping of Regimes”. In: *Fluidization Engineering (Second Edition)*. Ed. by Kunii Levenspiel. Second Edition. Boston: Butterworth-Heinemann, 1991, pp. 61–94. ISBN: 978-0-08-050664-7. DOI: http://dx.doi.org/10.1016/B978-0-08-050664-7.50009-3.

[25] Daizo Kunii and Octave Levenspiel. “Chapter 4 - The Dense Bed: Distributors, Gas Jets, and Pumping Power”. In: *Fluidization Engineering (Second Edition)*. Ed. by Kunii Levenspiel. Second Edition. Boston: Butterworth-Heinemann, 1991, pp. 95–114. ISBN: 978-0-08-050664-7. DOI: http://dx.doi.org/10.1016/B978-0-08-050664-7.50009-3.

[26] E. Kreyszig. *Advanced Engineering Mathematics*. John Wiley & Sons, 2010. ISBN: 9780470458365.

A

Appendix A

PSD data

Table A.1: PSD Data non-sieved

		[Sand:F]	[Ilm:F]	[Tierga:F]	[Buri:F]	[C14:F]	[Mesa:F]	[SinFin:F]
Mean $x_{50,3}$	[µm]	132,36	218,35	160,33	158,82	151,36	238,58	195,41
Sauter d_{32}	[µm]	97,55	155,23	116,77	84,57	113,06	151,61	139,79
Spread σ_{PSD}	[µm]	35,90	77,59	35,30	60,09	31,32	96,76	55,83
Fines	[%]	0,00	0,06	0,91	8,07	0,40	0,57	0,29

		[Ilm :10kW]	[Tierga :100kW]	[IlmBuri :100kW]	[C14 :10kW]	[Mesa :10kW]	[SinFin :100kW]	[Ilm :100kW,Filter]	[Tierga :Fines]
Mean $x_{50,3}$	[µm]	180,46	181,12	190,24	125,18	273,24	162,37	152,29	96,00
Sauter d_{32}	[µm]	119,61	132,06	140,16	83,26	179,05	108,30	78,93	69,57
Spread σ_{PSD}	[µm]	58,21	60,53	45,64	34,87	106,27	48,62	69,71	25,47
Fines	[%]	1,88	0,17	0,40	4,06	0,23	2,17	8,17	1,43

Table A.2: PSD Data sieved

		[Sand:F:S]	[Ilm:F:S]	[Tierga:F:S]	[Buri:F:S]	[C14:F:S]	[Mesa:F:S]	[SinFin:F:S]
Mean $x_{50,3}$	[µm]	138,72	197,50	161,67	171,32	152,36	196,84	196,18
Sauter d_{32}	[µm]	106,10	147,72	124,02	127,85	117,31	141,45	145,08
Spread σ_{PSD}	[µm]	30,95	48,90	32,30	45,33	29,11	59,79	51,47
Fines	[%]	-	-	-	-	-	-	-

		[Ilm :10kW:S]	[Tierga: :100kW:S]	[IlmBuri: :100kW:S]	[C14 :10kW:S]	[Mesa :10kW:S]	[SinFin: :100kW:S]	[Ilm:100kW, :Filter:S]	[Tierga: :Fines:S]
Mean $x_{50,3}$	[µm]	182,12	170,44	189,34	131,80	204,53	166,54	169,44	113,39
Sauter d_{32}	[µm]	136,24	131,41	144,88	102,3141357	150,45	125,85	127,42	89,83
Spread σ_{PSD}	[µm]	46,19	31,96	38,51	23,83	54,35	39,89	42,37	12,17
Fines	[%]	-	-	-	-	-	-	-	-

B

Appendix B

Score data

Table B.1: Experimental Outcome - non-sieved fresh

		[Sand:F]	[Ilm:F]	[Tierga:F]	[Buri:F]	[C14:F]	[Mesa:F]	[SinFin:F]
AOR	[°]	31,65	35,47	35,75	36,47	29,64	34,67	35,89
Flow	[ml/s]	3,25	4,55	4,32	3,92	5,76	4,44	4,38
HR	[-]	1,210	1,190	1,239	1,212	1,129	1,187	1,181

Table B.2: Scores - non-sieved fresh

		[Sand:F]	[Ilm:F]	[Tierga:F]	[Buri:F]	[C14:F]	[Mesa:F]	[SinFin:F]
AOR Score	[-]	0,92	-0,47	-0,57	-0,83	1,65	-0,18	-0,62
Flow Score	[-]	-0,97	-0,08	-0,24	-0,51	0,74	-0,16	-0,20
HR Score	[-]	-0,24	0,25	-0,94	-0,30	1,74	0,32	0,48
$\sum$		-0,29	-0,30	-1,75	-1,64	4,13	-0,01	-0,34

Table B.3: Experimental Outcome - non-sieved used

		[Ilm :10kW]	[Tierga :100kW]	[IlmBuri :100kW]	[C14 :10kW]	[Mesa :10kW]	[SinFin :100kW]	[Ilm :100kW,Filter]	[Tierga :Fines]
AOR	[°]	33,78	33,70	34,12	31,60	36,67	34,02	33,73	35,05
Flow	[ml/s]	4,87	4,74	5,16	3,43	4,31	4,94	4,37	3,70
HR	[-]	1,203	1,193	1,164	1,180	1,222	1,200	1,192	1,243

Table B.4: Scores - non-sieved used

		[Ilm :10kW]	[Tierga :100kW]	[IlmBuri :100kW]	[C14 :10kW]	[Mesa :10kW]	[SinFin :100kW]	[Ilm :100kW,Filter]	[Tierga :Fines]
AOR Score	[-]	0,14	0,17	0,02	0,94	-0,90	0,06	0,16	-0,32
Flow Score	[-]	0,14	0,04	0,33	-0,84	-0,25	0,18	-0,20	-0,66
HR Score	[-]	-0,06	0,18	0,88	0,51	-0,54	-0,01	0,19	-1,04
$\sum$		0,22	0,40	1,23	0,60	-1,69	0,23	0,16	-2,01

Table B.5: Experimental Outcome - sieved fresh

		[Sand:F:S]	[Ilm:F:S]	[Tierga:F:S]	[Buri:F:S]	[C14:F:S]	[Mesa:F:S]	[SinFin:F:S]
AOR	[°]	32,23	34,48	33,52	34,45	28,62	34,63	36,10
Flow	[ml/s]	4,18	4,25	4,66	4,21	5,46	4,46	4,41
HR	[-]	1,159	1,185	1,191	1,220	1,175	1,182	1,191

Table B.6: Scores - sieved fresh

		[Sand:F:S]	[Ilm:F:S]	[Tierga:F:S]	[Buri:F:S]	[C14:F:S]	[Mesa:F:S]	[SinFin:F:S]
AOR Score	[-]	0,71	-0,11	0,24	-0,10	2,02	-0,16	-0,70
Flow Score	[-]	-0,33	-0,28	-0,01	-0,31	0,54	-0,14	-0,17
HR Score	[-]	1,01	0,38	0,22	-0,50	0,61	0,46	0,23
$\sum$		1,39	-0,01	0,46	-0,90	3,16	0,15	-0,65

Table B.7: Experimental Outcome - sieved used

		[Ilm :10kW:S]	[Tierga :100kW:S]	[IlmBuri :100kW:S]	[C14 :10kW:S]	[Mesa :10kW:S]	[SinFin :100kW:S]	[Ilm:100kw, Filter:S]	[Tierga :Fines:S]
AOR	[°]	33,93	33,02	33,77	25,60	33,65	34,23	33,33	34,42
Flow	[ml/s]	4,34	4,70	4,78	6,15	4,53	4,44	4,46	4,39
HR	[-]	1,196	1,172	1,181	1,133	1,193	1,199	1,192	1,206

Table B.8: Scores - sieved used

		[Ilm :10kW:S]	[Tierga :100kW:S]	[IlmBuri :100kW:S]	[C14 :10kW:S]	[Mesa :10kW:S]	[SinFin :100kW:S]	[Ilm:100kW, Filter:S]	[Tierga :Fines:S]
AOR Score	[-]	0,09	0,42	0,15	3,11	0,19	-0,02	0,31	-0,09
Flow Score	[-]	-0,22	0,02	0,07	1,00	-0,10	-0,15	-0,14	-0,19
HR Score	[-]	0,11	0,69	0,46	1,64	0,18	0,03	0,20	-0,14
$\sum$		-0,03	1,13	0,68	5,75	0,28	-0,14	0,36	-0,41

C

Appendix C

Score (AOR, Flow, HR, u_{mf})

Alternatively a score was calculated which incorporates the minimum fluidization velocity to some extent. Concerning the u_{mf} density and particle size have obviously an important influence. By weighting u_{mf} according to C.1, an attempt was made to neglect this influence.

$$u^*_{mf} = \frac{u_{mf}}{x^2_{50,3} \cdot \rho_{particle}} \tag{C.1}$$

Establishing the score followed the procedure of chapter 4. Following lines are added to the tables 4.1 - 4.3:

Table C.1: Values for derivation of the flowability score

		[Sand:F]	[Ilm:F]	[Tierga:F]	[C14:F]	[Mesa:F]	[SinFin:F]
u^*_{mf}	[m^2/(kg s)]	305,2	341,4	370,7	526,8	348,4	332,9

Table C.2: Mean and standard deviation

		Mean μ	σ
u^*_{mf}	[m^2/(kg s)]	369	76

Table C.3: Scores

	[Sand:F]	[Ilm:F]	[Tierga:F]	[C14:F]	[Mesa:F]	[SinFin:F]
u^*_{mf} [m^2/(kg s)]	0,84	0,37	-0,02	-2,07	0,27	0,48
Score (AOR, Flow, HR)	-0,29	-0,3	-1,77	4,19	-0,01	-0,35
Score (AOR, Flow, HR, u_{mf})	0,55	0,06	-1,79	2,12	0,26	0,13

u_{mf} scores are assigned with a negative sign, since an increased u^*_{mf} means a higher effort for fluidization and thus indicates worse flowability. Figure C.1 and figure C.2 depicts the results from the alternative score.

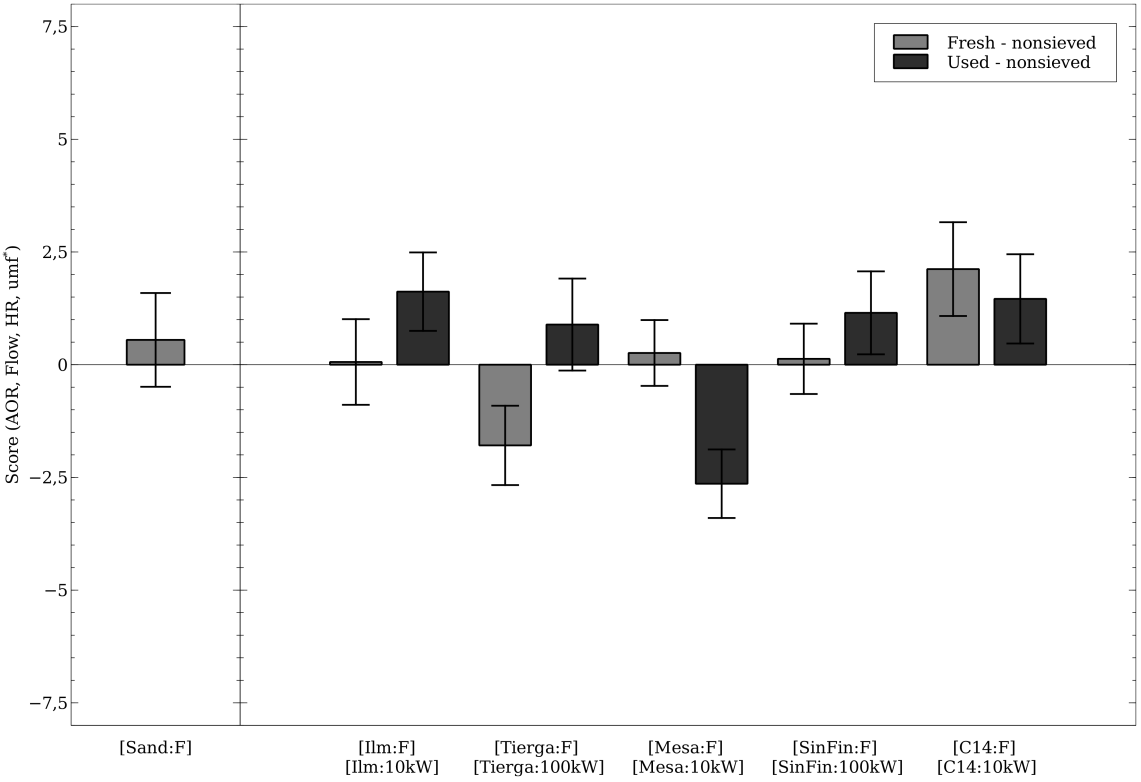

Figure C.1: Flowability score (AOR, Flow, HR, u_{mf})

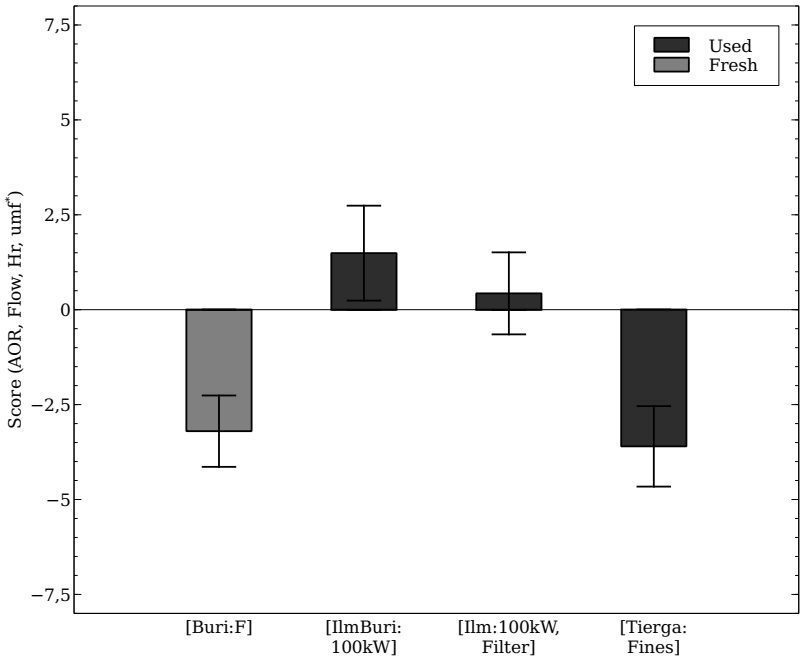

Figure C.2: Flowability score (AOR, Flow, HR, u_{mf})